

Non-local electrodynamics in ultra-pure PdCoO₂

Graham Baker,^{1,2} Timothy W. Branch,^{1,2} J. S. Bobowski,^{1,2,3} James Day,^{1,2} Davide Valentini,^{4,5}
Mohamed Oudah,¹ Philippa McGuinness,⁶ Seunghyun Khim,⁶ Piotr Surówka,^{7,8,9} Yoshiteru
Maeno,^{10,3} Roderich Moessner,¹¹ Jörg Schmalian,^{4,5} Andrew P. Mackenzie,^{6,12} and D. A. Bonn^{1,2}

¹*Stewart Blusson Quantum Matter Institute, University of British Columbia, Vancouver, British Columbia, Canada V6T 1Z4*

²*Department of Physics and Astronomy, University of British Columbia, Vancouver, British Columbia, Canada V6T 1Z1*

³*Department of Physics, Kyoto University, Kyoto 606-8502, Japan*

⁴*Institute for Theory of Condensed Matter, Karlsruhe Institute of Technology, Karlsruhe 76131, Germany*

⁵*Institute for Quantum Materials and Technologies,*

Karlsruhe Institute of Technology, Karlsruhe 76131, Germany

⁶*Max Planck Institute for Chemical Physics of Solids, Nöthnitzer Straße 40, 01187 Dresden, Germany*

⁷*Department of Theoretical Physics, Wrocław University of Science and Technology, 50-370 Wrocław, Poland*

⁸*Institute for Theoretical Physics, University of Amsterdam, 1090 GL Amsterdam, The Netherlands*

⁹*Dutch Institute for Emergent Phenomena (DIEP),*

University of Amsterdam, 1090 GL Amsterdam, The Netherlands

¹⁰*Toyota Riken - Kyoto University Research Center (TRiKUC), Kyoto 606-8501, Japan*

¹¹*Max Planck Institute for the Physics of Complex Systems, Nöthnitzer Straße 38, 01187 Dresden, Germany*

¹²*Scottish Universities Physics Alliance, School of Physics and Astronomy,
University of St Andrews, St Andrews KY16 9SS, United Kingdom*

(Dated: March 2, 2023)

The motion of electrons in the vast majority of conductors is diffusive, obeying Ohm's law. However, the recent discovery and growth of high-purity materials with extremely long electronic mean free paths has sparked interest in non-ohmic alternatives, including viscous and ballistic flow. Although non-ohmic transport regimes have been discovered across a range of materials, including two-dimensional electron gases, graphene, topological semimetals, and the delafossite metals, determining their nature has proved to be challenging. Here, we report on a new approach to the problem, employing broadband microwave spectroscopy of the delafossite metal PdCoO₂ in three distinct sample geometries that would be identical for diffusive transport. The observed differences, which go as far as differing power laws, take advantage of the hexagonal symmetry of PdCoO₂. This permits a particularly elegant symmetry-based diagnostic for non-local electrodynamics, with the result favoring ballistic over strictly hydrodynamic flow. Furthermore, it uncovers a new effect for ballistic electron flow, owing to the highly faceted shape of the hexagonal Fermi surface. We combine our extensive dataset with an analysis of the Boltzmann equation to characterize the non-local regime in PdCoO₂. More broadly, our results highlight the potential of broadband microwave spectroscopy to play a central role in investigating exotic transport regimes in the new generation of ultra-high conductivity materials.

There has been significant recent interest in unconventional electronic transport regimes in conductors in which a local relationship between electric current and electric field, as described by Ohm's law, breaks down. In the absence of frequent momentum-relaxing (MR) scattering, non-local effects can develop: when momentum-conserving (MC) scattering is sufficiently frequent, electrons flow collectively as a viscous fluid; when neither form of scattering is frequent, electrons propagate ballistically. While viscous and ballistic effects are conceptually distinct, they can lead to similar experimental signatures [1], making it dangerous to interpret experiments by comparing to theory rooted in one origin or the other. Additional impetus for comparing to theory incorporating both effects comes from the expectation that the hierarchy of scattering rates in most ultra-pure materials places them near the ballistic-to-viscous crossover, rather than at an extreme. Adding to the complexity, while early experiments and theories were based on materials with isotropic Fermi surfaces [2, 3], a recent theoretical focus has been extending these ideas to anisotropic sys-

tems [4–7]. Many questions remain unresolved, however, and it is vital to extend the range of experimental tools with which to investigate these new transport regimes.

To date, the vast majority of work has been performed in the DC limit. The reason for this is the difficulty of performing broadband AC experiments in the GHz region of the spectrum; as we will discuss in more detail below, this is an area in which theory has been ahead of experiment, with predictions for the expected frequency dependence in different non-local regimes, but no actual data for comparison. In this paper, we explore this frequency-dependent physics using unique, bespoke experimental apparatus: a broadband bolometric microwave spectrometer [8]. We report results from a number of ultra-pure metals over 1.5 decades of frequency, from 0.6 to 20 GHz. Through measurements on Sr₂RuO₄ and Sn, we verify the predictions for the frequency dependence of the surface resistance for the Classical and Anomalous Skin Effects. Data from the ultra-pure delafossite PdCoO₂, in contrast, deviate from any previous prediction of frequency-dependent surface resistance. Analysis

of such data required the construction of a more complete electrodynamic theory of metals than previously existed, and allows us to conclude that the PdCoO_2 data are due to the combination of a highly anisotropic Fermi surface and a contribution from momentum-conserving scattering.

The paper is organized as follows: after introducing our broadband bolometric technique in Section I, we discuss the AC electrodynamics of high-purity metals in Section II, and results from Sr_2RuO_4 and Sn in Section III. We then review what is known about non-local transport in PdCoO_2 in Section IV, before presenting and analyzing its broadband AC response in Section V. We close the paper with Section VI, discussing the implications of these results and the future role that AC measurements can play in the study of unconventional transport regimes in metals.

I. MICROWAVE SPECTROSCOPY

Differentiating between non-local effects requires transport measurements on length scales comparable to the MR and MC mean free paths, λ_{mr} and λ_{mc} . To date, this has been approached by studying how DC transport properties vary with the dimensions of micro-structured samples. Here we take a new approach by measuring the AC properties of bulk samples, using the skin effect to impose a *tunable* length scale, the skin depth. In any metal, AC electromagnetic fields decay as they propagate. The result is that the electromagnetic fields—and resulting current density—are confined to a “skin layer” at the surface. A key advantage to AC measurements, in principle, is that this skin depth is frequency dependent: the DC approach necessitates additional fabrication each time sample dimensions are varied, but AC measurements offer the possibility of continuously varying the skin depth. Although conceptually simple, this requires broadband measurement over the microwave range of the spectrum.

Microwave frequencies fall between the range of conventional electrical and optical techniques, presenting a unique challenge for broadband spectroscopy—particularly for high-conductivity samples [8–10]. While reflectivity measurements are commonly used at higher frequencies, at microwave frequencies two difficulties arise: (1) the free-space wavelength becomes comparable to or greater than typical sample dimensions, leading to diffraction, and (2) the reflectivity of high-conductivity metals becomes indistinguishable from unity. At lower frequencies, electrical leads are attached directly to the sample. However, the impedance of high-conductivity samples at microwave frequencies is on the order of $\text{m}\Omega$ —much lower than typical values of either contact resistance or transmission line impedance.

The most widely-adopted technique at microwave frequencies is cavity perturbation, in which a sample’s electromagnetic properties are measured via its effect when

introduced into a high- Q resonator. Cavity perturbation achieves high sensitivity by amplifying the sample-radiation interaction through repeated reflections. However, the technique suffers the drawback of being at a fixed frequency. As will be discussed in the following section, this eliminates a key means of distinguishing between electrodynamic regimes and necessitates the use of restrictive assumptions when interpreting data.

Here, we report the use of a bespoke technique giving us the capability of covering the range from 0.6 to 20 GHz continuously [8]. The basis of the technique is a bolometric measurement of the power absorbed by the sample from microwave electromagnetic fields, which is proportional to its surface resistance. Compared to other approaches to spectroscopic measurements at microwave frequencies [11, 12], our technique is uniquely capable of resolving non-local effects in high-purity metals as a result of three distinct technical advantages: (1) We achieve high-sensitivity bolometric detection via a miniaturized thermal stage, careful thermometer selection, and home-built signal conditioning electronics. This provides us the sensitivity and dynamic range necessary to cover different skin effect regimes. (2) We use a custom-made transmission line to achieve a contactless, uniform, and well-defined microwave field configuration. This permits the separation of anisotropic components and gives us flexibility of measurement geometry—as we shall see, the geometric requirements are even more stringent for non-local versus local measurements. (3) We use an in-situ reference sample to measure the microwave field strength at the sample, eliminating frequency-dependent standing-wave effects and yielding an absolute calibration. Taken together, these technical advantages give us the unprecedented and unmatched ability to measure non-local electrodynamics in anisotropic, ultra-pure metals.

II. NON-LOCAL ELECTRODYNAMICS OF METALS

The skin effect takes several forms depending on the nature of the electron dynamics within the skin layer, each characterized by unique frequency dependence and symmetry constraints of the AC surface resistance. Mathematically, electromagnetic propagation can be conveniently described via a propagator \mathcal{A} which depends on wavevector q and frequency ω :

$$\mathcal{A}_{ij}(\mathbf{q}, \omega) = \frac{\mu_0}{i\mu_0\omega\sigma_{ij} + \omega^2/c^2 - q^2}. \quad (1)$$

The poles of \mathcal{A} are solutions to Maxwell’s equations and give the dispersion relations $q(\omega)$ governing the propagation of electromagnetic modes within the metal. The effect of a metal’s conductivity σ is to increase the wavevector and to induce an imaginary component; the skin depth is given by $\delta = 1/\text{Im}(q)$.

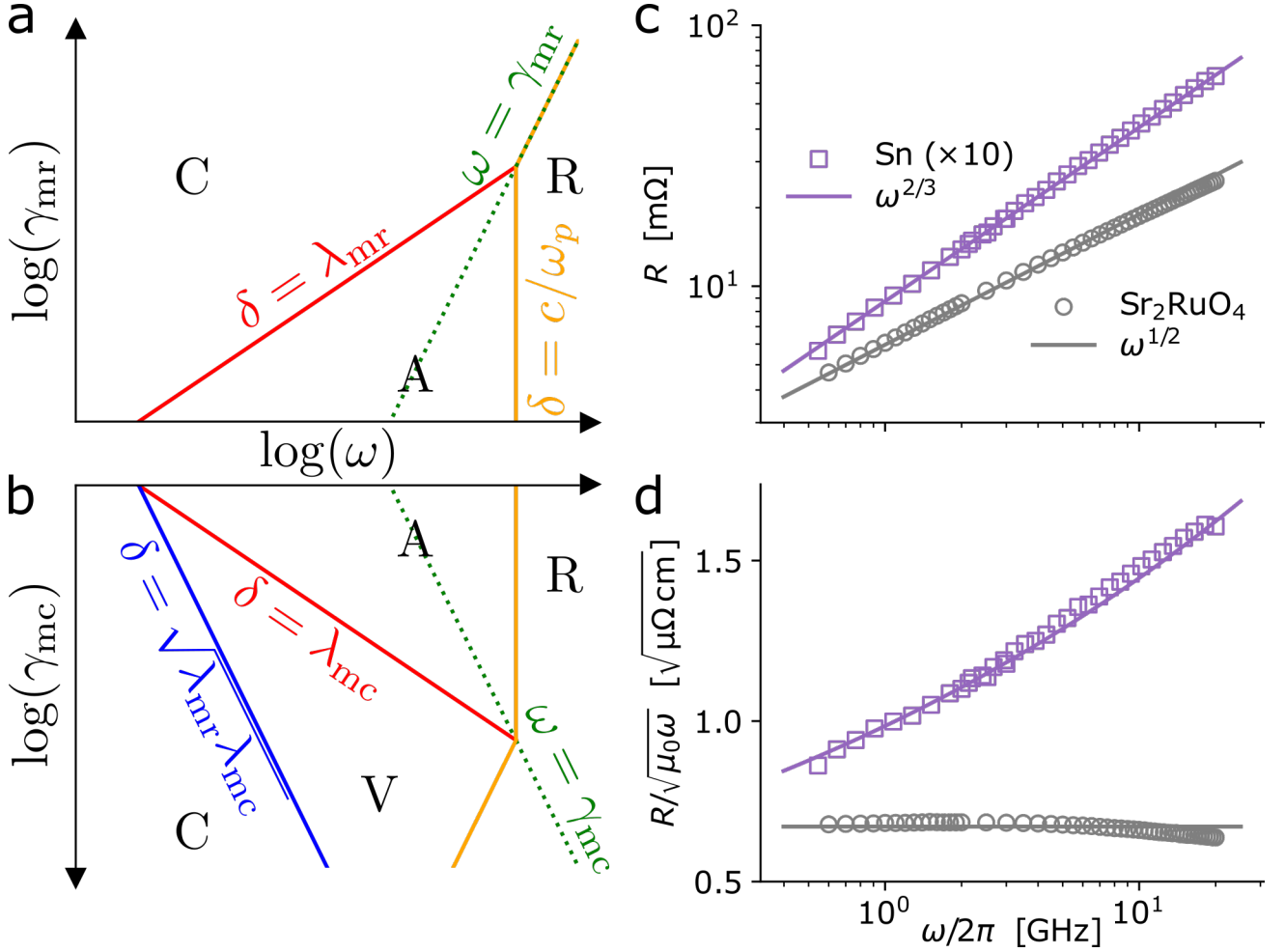


FIG. 1. (a),(b) Predicted skin effect regimes according to conventional theory as a function of frequency ω , momentum-relaxing scattering rate γ_{mr} , and momentum-conserving scattering rate γ_{mc} . (a) The transition from **C**lassical to **A**nomalous Skin Effect occurs when the momentum-relaxing mean free path λ_{mr} is longer than the skin depth δ . In this case, electrons propagate ballistically within the skin layer. (b) For sufficiently strong momentum-conserving scattering within the skin layer, a **V**iscous Skin Effect is predicted to emerge. To our knowledge, this has not yet been experimentally observed. In both (a) and (b), the **R**elaxation regime occurs at the highest frequencies, reflecting finite-frequency effects in the conductivity. (c),(d) Spectroscopic surface resistance measurements of Sr_2RuO_4 and Sn. (c) The power law behavior of $R(\omega)$ indicates that Sr_2RuO_4 exhibits the Classical Skin Effect while Sn exhibits the Anomalous Skin Effect. (d) Dividing R by $\sqrt{\omega}$ provides a sensitive visual test for deviations from classical $R \sim \sqrt{\omega}$ behavior.

In most metals, the relationship between the AC electric field and the induced current density is local—the electric current at a given point in space depends only on the electric field at that same point. This is expressed by Ohm’s law:

$$J_i(\mathbf{r}, \omega) = \sigma_{ij}(\omega) E_j(\mathbf{r}, \omega). \quad (2)$$

The reason Ohm’s law is valid is that frequent scattering randomizes an electron’s momentum on a scale much shorter than the variation of the decaying electric field. This gives rise to the Classical Skin Effect (CSE), for which surface resistance is directly related to the local

conductivity:

$$R_i(\omega) = \text{Re} \sqrt{\frac{i\mu_0\omega}{\sigma_{ii}(\omega)}}. \quad (3)$$

At low frequency, $R \sim \omega^{1/2}$. The symmetry of R is that of the local conductivity tensor σ_{ij} , which is set by the crystal system.

However, Ohm’s law cannot always be valid: in the absence of MR collisions, an electron’s momentum will depend on the entire history of the varying electric field along its trajectory. This can be resolved via a generalized, non-local version of Ohm’s law using a wavevector-dependent conductivity:

$$J_i(\mathbf{q}, \omega) = \sigma_{ij}(\mathbf{q}, \omega) E_j(\mathbf{q}, \omega). \quad (4)$$

In this case, R is a wavevector-integrated function of the non-local conductivity, gaining an additional source of anisotropy via the direction of the wavevector \mathbf{q} :

$$R_{i,\mathbf{q}}(\omega) = \text{Re} \int d\mathbf{q} \mathcal{A}_{ii}(\mathbf{q}, \omega). \quad (5)$$

An established instance of non-local electrodynamics is the Anomalous Skin Effect (ASE), in which electrons propagate ballistically within the skin layer. The ASE is expected to occur when $\delta \ll \lambda_{\text{mr}}$ (as marked by the red line in Fig. 1(a)), and is predicted to exhibit a surface resistance that becomes independent of the bulk conductivity and whose magnitude exceeds the CSE expectation [13–15]. The ASE has been observed experimentally at low temperature in a select number of high-purity elemental metals [16–19], though always at one fixed frequency. It has also long been predicted that surface resistance follows $\omega^{2/3}$ behavior in the ASE [13–15]. To our knowledge, while this frequency dependence has been assumed in the interpretation of fixed-frequency measurements, it has never been measured directly.

Another instance of non-local electrodynamics—the Viscous Skin Effect (VSE)—is predicted to occur in an intermediate regime $\sqrt{\lambda_{\text{mr}}\lambda_{\text{mc}}} \ll \delta \ll \lambda_{\text{mc}}$ (as shown by the blue and red lines in Fig. 1(b)) and is characterized by $\omega^{3/4}$ behavior [20]. To our knowledge, it has not yet been observed experimentally.

The upper frequency boundary for all of the above skin effects is determined by the onset of the relaxation regime, in which the conductivity leaves the zero-frequency limit. This boundary is given by $\delta = c/\omega_p$ where c is the vacuum speed of light and ω_p is the plasma frequency, as marked by the orange line in Fig. 1(a) and (b). For local electrodynamics, this aligns with the conventional Drude criterion $\omega = \gamma_{\text{mr}}$, shown by the dashed green line in Fig. 1(a).

III. MEASUREMENTS ON Sr_2RuO_4 AND Sn

To set the stage for discussing more complex behavior, we begin by showing spectroscopic measurements of single-crystal Sr_2RuO_4 and polycrystalline Sn in Fig. 1(c) and (d). Both measurements were taken using our unique, home-built spectrometer and slightly above the respective superconducting transition temperatures. The Sr_2RuO_4 data, taken at 2.6 K, exhibits the $\omega^{1/2}$ behavior expected for the CSE. The magnitude of a CSE fit gives an in-plane resistivity of approximately 50 n Ω cm, consistent with that of the highest-quality samples as measured by conventional DC four-point electrical measurements [21, 22]. As a consistency check, the measured resistivity value implies that the conditions $\delta < \lambda_{\text{mr}}$ and $\omega < \gamma_{\text{mr}}$ are met over our measurement frequencies, meaning that we should indeed expect to observe the CSE [23]. The Sn data, taken at 5.0 K, exhibits the $\omega^{2/3}$ behavior expected for the ASE. The magnitude of an ASE fit gives a Fermi velocity of of 2.2×10^6 m/s [23], within 20% of

the published value of 1.9×10^6 m/s [24]. Because the ASE surface resistance is insensitive to the MR scattering rate, in this case we cannot directly use the information from our fit to compute the expected skin effect boundaries. However, for $\delta = \lambda_{\text{mr}}$ to be satisfied over our measurement range implies an upper bound on γ_{mr} , values below which are known to be achievable in high-purity Sn [16][23]. To our knowledge, this is the first ever spectroscopic measurement of the ASE, confirming the frequency dependence predicted by theory [13–15]. Since we will be concerned mainly with departures from the CSE, we introduce a plot that emphasizes deviation from this simple $\sqrt{\omega}$ behavior. In Fig. 1(d), we plot the same data sets, but rescaled by $\sqrt{\omega}$. For Sr_2RuO_4 , the result is quite flat, as expected for the CSE; for Sn, there is a clear upward trend. These measurements highlight our ability to make precise measurements over a broad frequency range, confirming existing theory both in frequency dependence and in absolute magnitude.

IV. DC EVIDENCE FOR NON-LOCAL TRANSPORT IN PdCoO_2

Having established the capability of our spectroscopic technique to differentiate between transport regimes, we now turn our attention to measurements of PdCoO_2 , whose crystal structure is shown in Fig. 2(a). This material is of considerable interest for AC conductivity measurements because DC studies indicate that it has extremely high purity [25, 26] and shows signatures of non-local transport. Initial analysis of the dependence of its resistivity on channel width suggested viscous corrections to ballistic transport [27] but the data were analyzed using models previously employed to study non-ohmic transport in two-dimensional electron gases, in which a circular Fermi surface was assumed [2, 3]. The real Fermi surface of PdCoO_2 (Fig. 2(b)) is nearly cylindrical, as expected for a nearly two-dimensional metal, but has a faceted, nearly hexagonal cross-section [25, 28, 29]. Although this makes no difference to the local DC transport properties at high temperatures, when a non-local DC transport regime is entered, strong directional effects are seen. Specifically, devices of a given geometry yield different responses depending on their orientation relative to the Fermi surface facets [30–32]. To date, the combined role of directional and viscous effects in PdCoO_2 has not been analyzed. This background motivated us to investigate whether the AC response of PdCoO_2 might be even richer than that predicted for the usual ASE, and provide new insight into the physics of PdCoO_2 .

V. MEASUREMENTS ON PdCoO_2

Our measurements were performed at 2 K so as to match previous non-local DC transport studies [27, 30–32]. At this temperature, published values imply that

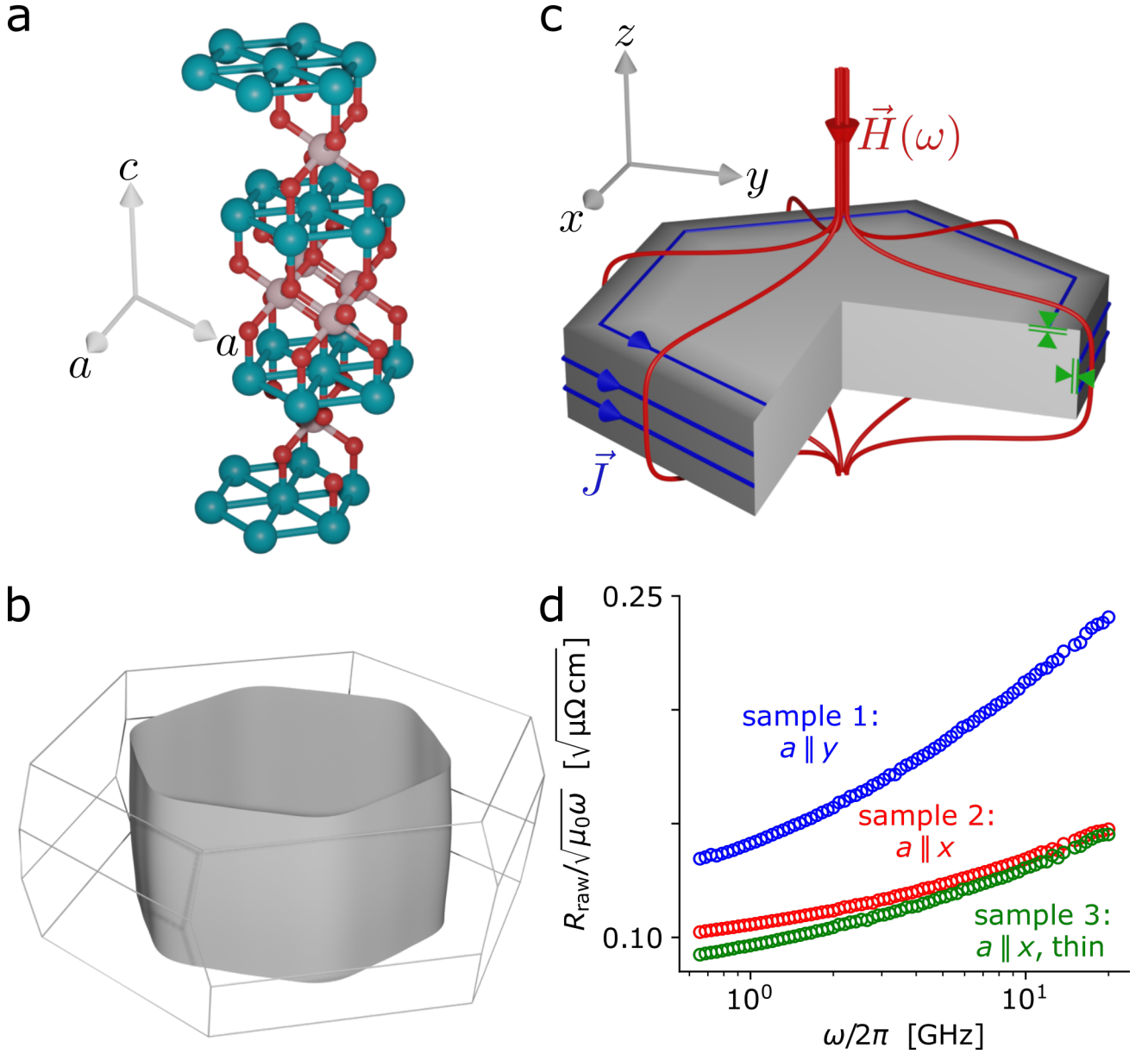


FIG. 2. (a) PdCoO₂ crystal structure, belonging to the trigonal crystal system. (b) PdCoO₂'s hexagonally faceted Fermi surface, as determined via ARPES and quantum oscillations [25]. (c) Measurement geometry. Samples, which grow naturally as thin platelets, were cut into hexagons to reflect the 6-fold rotational symmetry of the crystal structure. A microwave-frequency magnetic field is applied along z . This induces eddy currents (blue) acting to screen the magnetic field (red) from the interior of the sample. The resulting field strength at the sample's surface (grey shading) is highest on the side faces but also becomes appreciable toward the edges of the top and bottom faces. Because the skin depth is much smaller than the sample dimensions, this gives rise to two separate “skin regions” (indicated by green arrows). In both, current flows in the (001) plane and the wavevector is perpendicular to the surface. The measured signal contains a mixture of the two skin regions that depends on the sample's aspect ratio. (d) Raw data. We measured three samples, with two different cut orientations and two different aspect ratios. When the sample is cut with $a \parallel x$, $\mathbf{q} \parallel \langle 110 \rangle$ (“30”) on the side faces; when the sample is cut with $a \parallel y$, $\mathbf{q} \parallel \langle 100 \rangle$ (“0”) on the side faces. Varying the aspect ratio enables isolating the contribution from the top and bottom faces, where $\mathbf{q} \parallel c$. All three measurements differ—by symmetry, this can only occur for non-local electrodynamics.

the skin depth in our frequency range satisfies $c/\omega_p \ll \delta \ll \lambda_{\text{mr}}$. This is an ideal regime for our investigation; for a single scattering rate, we would expect to observe the ASE; for sufficient MC scattering, we would be in a position to observe the VSE. The faceted Fermi sur-

face of Fig. 2(b) immediately suggests three extremal wavevector directions for which to perform measurements: $\mathbf{q} \parallel \langle 100 \rangle$ (“0”), $\mathbf{q} \parallel \langle 110 \rangle$ (“30”), and $\mathbf{q} \parallel \langle 001 \rangle$ (“c”). Samples of PdCoO₂ grow as platelets with in-plane dimensions around 1 mm and typical thicknesses

of tens of microns. To reflect the underlying symmetry of the crystal structure, we cut samples to have hexagonal cross section, with lateral dimensions of about 0.5 mm (Fig. 2(c)). We applied a spatially-uniform, microwave-frequency magnetic field parallel to the c axis, inducing eddy currents which flow in loops perpendicular to the magnetic field. This establishes two distinct skin regions: one for currents on the two large hexagonal faces, with wavevector along the c axis, and the other for currents on the six small rectangular faces, with wavevector perpendicular to the c axis. The hexagonal cross section of the sample ensures that the wavevectors for each of the six rectangular faces are along symmetry equivalent directions. A measurement of a given sample thus contains a mixture of two distinct surface resistance components—with in- and out-of-plane wavevector directions—with weights depending on the sample’s aspect ratio. Our raw measurements are shown in (Fig. 2(d)). Sample 1 was cut with $a \parallel y$ so that the in-plane wavevector had $\mathbf{q} \parallel 0$; sample 2 was cut with $a \parallel x$ so that the in-plane wavevector had $\mathbf{q} \parallel 30$. Sample 3 was cut with the same orientation as sample 2, but was thinner, increasing the relative weight of the contribution from $\mathbf{q} \parallel c$. With measurements of these three samples, we obtained sufficient information to disentangle the surface resistance components for the three wavevector directions of interest. However, even without disentangling the components, the fact that the three raw measurements differ provides immediate evidence of non-local electrodynamics. For all three components, current flows in the plane perpendicular to the c axis; for local electrodynamics, the triangular in-plane lattice dictates that the conductivity tensor has no in-plane anisotropy and so all three components—and therefore the three raw measurements which mix them—would be identical. To proceed further, we used electromagnetic simulations to disentangle the surface resistance components for the three wavevector directions from the raw measurements of the three samples [23].

The measured surface resistance for the two in-plane wavevectors is shown in Fig. 3(a). Surprisingly, the two orientations exhibit distinct power-law behaviors. A useful property of the viscosity tensor in a plane with six-fold rotational symmetry provides an elegant avenue for differentiating ballistic and viscous effects: in this setting, as is the case in PdCoO₂, the in-plane viscosity tensor is isotropic [33]. This implies the qualitative insight that the anisotropy in the surface resistance at 2 K for the two orientations cannot be due to purely viscous effects.

With this in mind, we turn to the possible ballistic origin of this effect. The standard theory of the ASE (i.e., ballistic propagation within the skin layer)—Pippard theory [15]—predicts that any orientation should exhibit $R \sim \omega^{2/3}$, with only the pre-factor being orientation-dependent. Our data is at odds with Pippard theory: while one orientation exhibits behavior close to $\omega^{2/3}$, the other exhibits only a weak deviation from classical behavior. This breakdown of Pippard theory is all

the more surprising because—aside from its ubiquity—Pippard theory has previously demonstrated success in describing the behavior of anisotropic Fermi surfaces. Famously, Pippard performed the first ever experimental determination of a Fermi surface by applying his eponymous theory to measurements of the ASE in Cu, revealing deviation from a spherical Fermi surface [34]. Nonetheless, Pippard theory treats Fermi surface geometry phenomenologically, and was originally justified by agreement with more rigorous treatments based on solving the Boltzmann equation for spherical [13] and spheroidal [14] Fermi surfaces.

Clearly, we need to go further. To model our results, we solved the Boltzmann equation using a realistic, three-dimensional parameterization of the Fermi surface of PdCoO₂ based on ARPES and quantum oscillation measurements [25]. As seen in Fig. 3(a) and (b), our calculations qualitatively reproduce the difference in power-law behavior between the two orientations. An intuitive explanation for the difference in power laws comes from applying Pippard’s “ineffectiveness concept” [15, 16] to the Fermi surface of PdCoO₂ (Fig. 3(c)): only those electrons that spend an entirety of a mean free path within the skin layer are effective at screening electromagnetic fields. As the ratio of mean free path to skin depth increases, electrons spend an increasingly small fraction of a mean free path within the skin layer, so the surface resistance becomes increasingly larger than the classical value. Mathematically, this can be described as an effective mean free path for each state \mathbf{k} , which represents that state’s contribution to the overall conductivity:

$$\lambda_{\mathbf{k}}^{\text{eff}} = \frac{(\hat{\mathbf{v}}_{\mathbf{k}} \cdot \hat{\mathbf{E}})^2 \lambda_0}{1 + i(\hat{\mathbf{v}}_{\mathbf{k}} \cdot \hat{\mathbf{q}}) q \lambda_0} \quad (6)$$

where λ_0 is the bare mean free path and $\hat{\mathbf{v}}_{\mathbf{k}}$ is the unit velocity vector. (Because the present discussion is focused on purely ballistic effects, here we have taken $\lambda_{mr} = \lambda_{mc} = \lambda_0$). In PdCoO₂ in the lower orientation in Fig. 3(c), a third of electrons propagate nearly parallel to the sample’s surface, such that $\hat{\mathbf{v}}_{\mathbf{k}} \cdot \hat{\mathbf{q}} = 0$. These electrons remain effective at screening regardless of the ratio of mean free path to skin depth, largely suppressing the increase in surface resistance. Indeed, there have been several theoretical works predicting extreme Fermi surface geometries for which Pippard theory would break down [35–37]. To our knowledge, the present results represent the first experimental confirmation of these ideas.

The measured surface resistance for wavevector along the c axis, shown in Fig. 4(a), exhibits a clear deviation from classical $R \sim \sqrt{\omega}$ behavior. The observation of non-local electrodynamics in this orientation is surprising: as per the ineffectiveness concept, this means that electrons must be able to propagate in and out of the skin layer within a single mean free path. However, the nearly cylindrical geometry of the Fermi surface means that in this orientation, electrons propagate at a shallow angle relative to the skin layer (Fig. 4(c)). PdCoO₂ is often described as electronically two-dimensional or quasi-two-

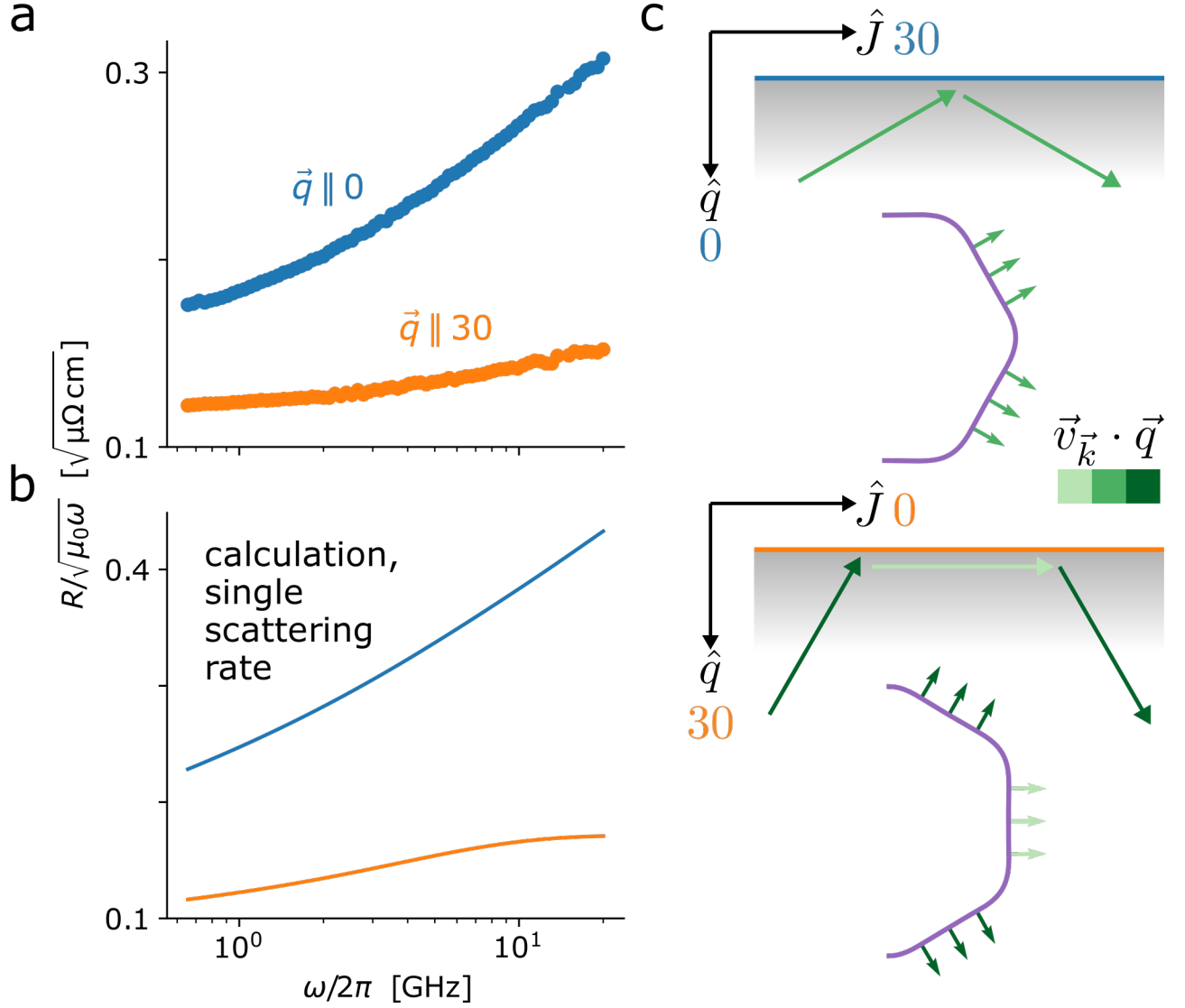


FIG. 3. (a) Surface resistance data with in-plane wavevector, obtained by subtracting the $\vec{q} \parallel c$ component from the raw measurements. The different power-law behavior originates from predominantly ballistic propagation within the skin layer coupled with a strongly-faceted Fermi surface, as illustrated in (b) and (c). (b) Calculated surface resistance based on the experimentally-determined Fermi surface, capturing the different power-law behavior of the two orientations. The calculation is for a single relaxation rate, i.e. $\gamma_{mc} = \gamma_{mr}$, and uses published values with no free parameters [23]. (c) Illustration of ballistic propagation within the skin layer. Top: There are two main directions of electron propagation, both at an angle to the surface. As frequency increases, the skin depth becomes shallower. The electrons spend an increasingly smaller fraction of a mean free path inside the skin layer, leading to an increasing surface resistance—the Anomalous Skin Effect. Bottom: There are three main directions of electron propagation. Electrons propagating parallel to the sample’s surface spend the entirety of a mean free path within the skin layer, regardless of how shallow the skin depth becomes. Often, this is a negligible fraction of the Fermi surface; in PdCoO₂, approximately a third of the Fermi surface propagates parallel to the sample’s surface. The Anomalous Skin E Effect is largely suppressed even when the mean free path is much larger than the skin depth.

dimensional, as supported by its low-temperature resistivity anisotropy of $\rho_c/\rho_a \approx 1000$ [25]. However, in a perfectly two-dimensional material, the ASE would be completely suppressed. Its presence here is a result of the subtle warping of the Fermi surface along k_z , as was resolved by quantum oscillations, and highlights the limitations of a purely two-dimensional description of transport properties in PdCoO₂. This observation has impli-

cations for DC transport measurements. To date, studies have focused on how resistivity varies when restricting in-plane dimensions; these results imply that size effects will also be present while varying thickness along the c axis. We estimate that the maximum skin depth over our measured frequency range is on the order of 100 nm. This implies that size effects are likely to be especially important to thin films, which have been the subject of

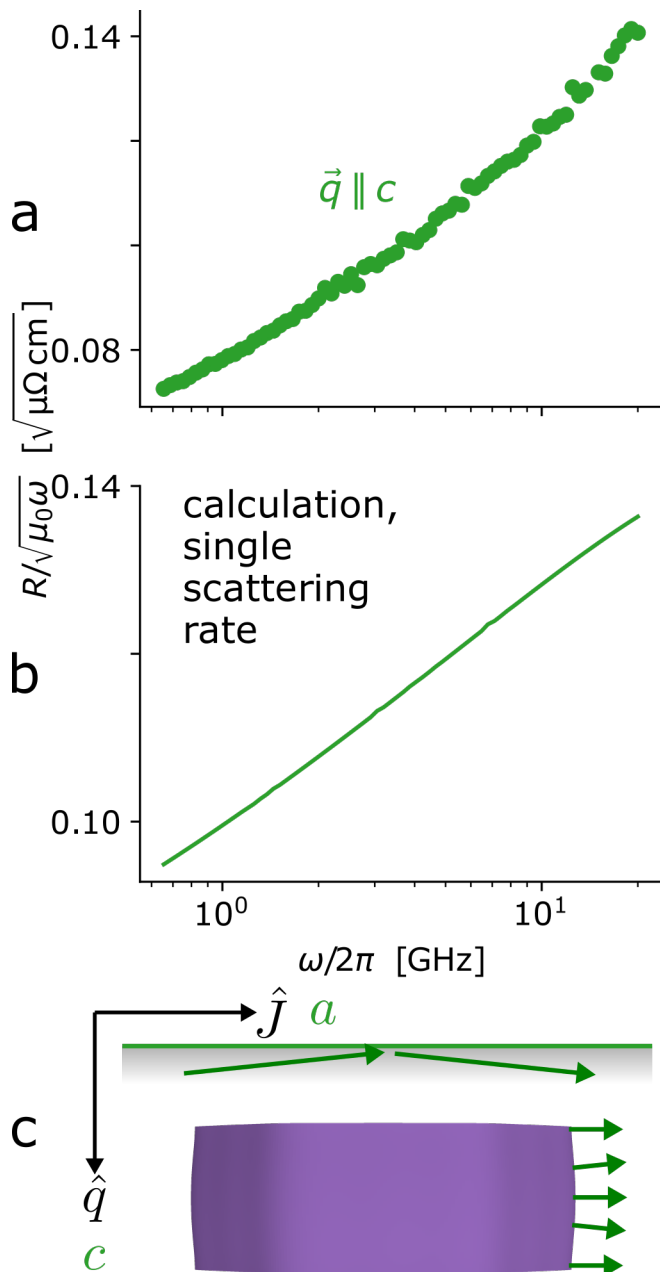


FIG. 4. (a) Surface resistance data with out-of-plane wavevector, obtained by comparing raw measurements from samples of different thicknesses. The data shows upward deviation from classical $R \sim \sqrt{\omega}$ behavior. Because of the high ratio of mean free path to skin depth reached toward the upper end of our frequency range, even the small amount of Fermi surface warping along k_z is sufficient to produce non-local effects. (b) Calculated surface resistance based on the experimentally-determined Fermi surface. The calculation is for a single relaxation rate, i.e. $\gamma_{mc} = \gamma_{mr}$, and uses published values with no free parameters [23]. (c) Illustration of ballistic propagation within the skin layer.

recent growth efforts [38–40].

Having identified a ballistic origin for the main features of the three measured surface resistances, we now turn to placing a quantitative bound on the rate of MC scattering. To do so, we developed a model that allows for arbitrary rates of MR and MC scattering. Combined with using a realistic, three-dimensional Fermi surface parameterization, these ingredients allow our model to encompass both directional and viscous effects. In Fig. 5, we compare the data for in-plane wavevector to calculations in which we no longer make our earlier assumption of a single relaxation rate. The only free parameter of these calculations is the MC scattering rate; the MR scattering rate and other material parameters are taken from the literature. As seen in Fig. 5(b), the higher the value of γ_{mc} , the lower the anisotropy between the two surface resistances. This is in accord with our earlier insight that deep in the viscous regime, symmetry dictates that there should be no anisotropy. The calculations for $\gamma_{mc}/\gamma_{mr} = 1$, shown previously, produce too much anisotropy. For $\gamma_{mc}/\gamma_{mr} = 30$, the isotropic, viscous limit is nearly reached. For intermediate values, a quantitative match to the data is achieved. From this comparison, we determined that $\gamma_{mc} = (7 \pm 3)\gamma_{mr}$ at 2 K. In Fig. 5(c) and (d), we show the calculated power-law behavior of the surface resistance over a wider range of frequency, showing the orientation-dependent modification of power-law behavior as well as the relation of our measurements to other skin effect regimes.

VI. DISCUSSION & OUTLOOK

The fact that our experiments are best matched by $\gamma_{mc} \approx 7\gamma_{mr}$ at 2 K is striking for several reasons. Firstly, it agrees within experimental error with the deduction made from the width dependence of DC transport in Ref. [27]. That DC measurement, however, was performed on a device of unknown orientation relative to the Fermi surface facets, and analyzed using the assumption of a circular Fermi surface cross-section, so the agreement may be fortuitous. We believe that the deduction we report here is on a firm footing because orientation and Fermi surface faceting have been taken carefully into account.

Secondly, the observation of a contribution from MC scattering raises the question of its source at this low temperature of 2 K. Given that $T \ll T_F$, it is expected that direct electron-electron scattering is negligible, even taking into account an enhanced cross-section due to Fermi surface faceting [4]. A recent work has proposed a phonon-mediated electron-electron interaction as a source of sufficient MC scattering [42], but such a mechanism—indeed any mechanism invoking electron-electron scattering—would be predominantly MR in PdCoO_2 due to Umklapp processes. While electron-phonon processes can in principle be a source of MC scattering [27, 43, 44], we estimate that it is insufficient to give rise to our experimentally-determined value of γ_{mc} [23], and there is no sign in DC

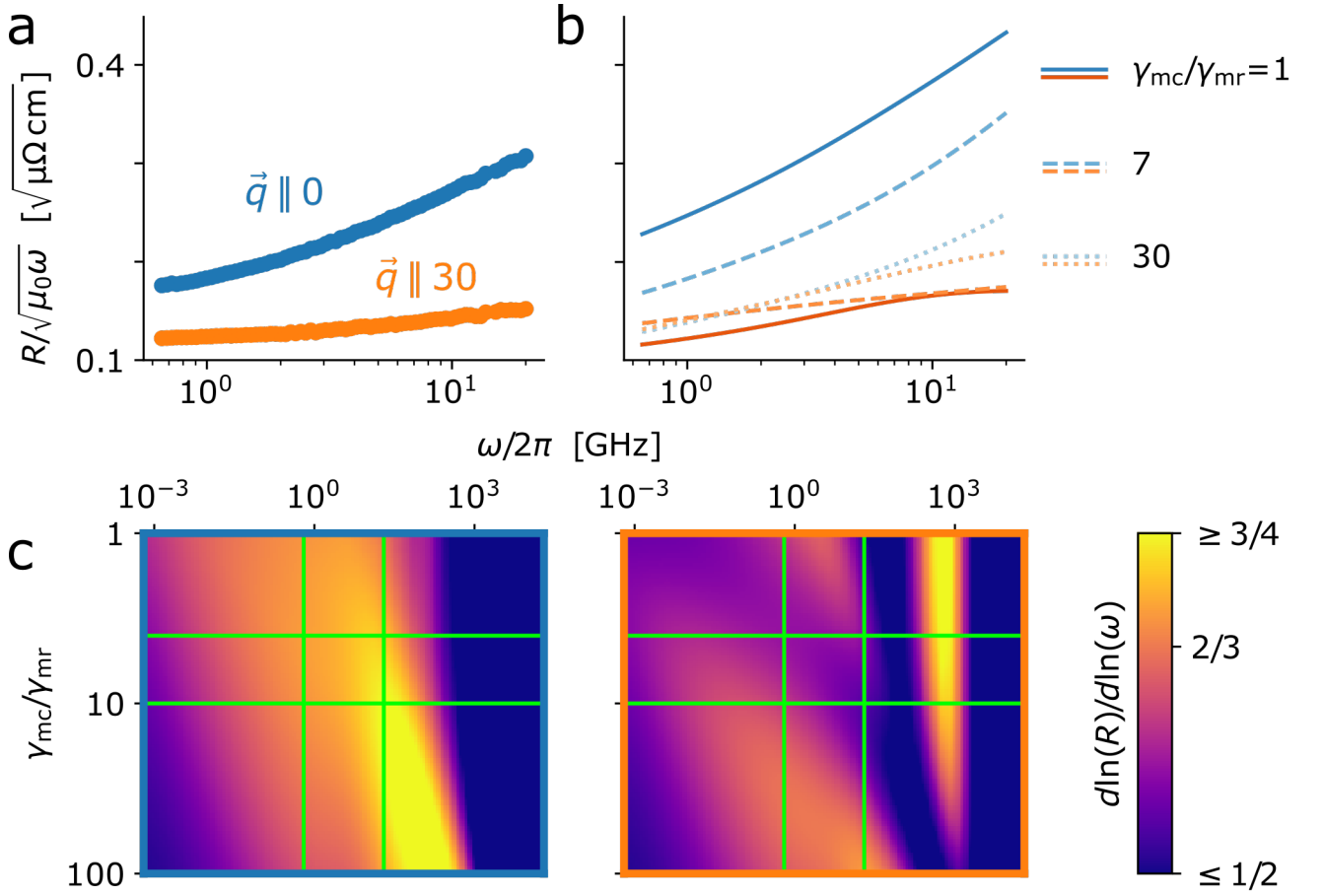


FIG. 5. Determination of momentum conserving scattering rate. (a) Experimental data for in-plane wavevector, on the same scale as (b). (b) Calculated surface resistance for various values of γ_{mc} , with γ_{mr} and all other parameters fixed by their literature values [41]. For $\gamma_{mc}/\gamma_{mr} = 1$, corresponding to the conventional relaxation time approximation, the calculated anisotropy between the two surface resistances is too large. For $\gamma_{mc}/\gamma_{mr} = 30$, the anisotropy is too small; the two surface resistances are almost equal, as expected deep in the viscous regime. For our best fit value of $\gamma_{mc}/\gamma_{mr} = 7$, a quantitative match is achieved. (c),(d) Calculated surface resistance for (c) $R_{a,\vec{q} \parallel 0}$ and (d) $R_{a,\vec{q} \parallel 30}$ over a broader range of frequency and momentum-conserving scattering rate. Vertical green lines show our measurement range while horizontal green lines show our finding that γ_{mc}/γ_{mr} is between 4 and 10. The color plot shows the power-law behavior of the surface resistance, showing its orientation-dependent modification as well as where our measurements fit relative to other skin effect regimes.

measurements at temperatures below 10 K of the strong temperature dependence predicted in such scenarios. Instead, the low temperature of our measurements is suggestive of impurity scattering as the source of the observed γ_{mc} [4]. While recent theoretical work has begun to explore the connection between electron-impurity scattering and MC scattering [45], these experimental observations motivate further theoretical work to establish whether this explanation is realistic in the present setting.

The results presented in this paper have future implications both for understanding the physics of PdCoO₂ and for the broader field of non-local effects in ultra-clean metals. For the first time, we have combined experiment and analysis to investigate the combined effects of momentum-conserving scattering and Fermi surface anisotropy—including both the effect of in-plane faceting

and out-of-plane warping. In PdCoO₂ and other delafosites, the existence of Boltzmann transport code capable of working with realistic Fermi surface parameterizations will enable further in-depth investigation of the balance between MC and MR scattering in both the AC and DC regimes. By extending the range of frequencies over which there is information to 20 GHz and showing the unconventional frequency dependencies revealed in our measurements, we have provided a stringent test for this analysis model. Its ability to reproduce those frequency dependencies gives more confidence in its correctness (and in the assumptions on which it is based) than could ever be achieved from DC data alone. While Refs. [30–32] showed that Fermi surface geometry and orientation can have an effect on non-local transport, here we have shown that they can go as far as modifying the power-law relationship between transport prop-

erties and an imposed, extrinsic lengthscale. Both in the skin effect and the size effect in narrow channels, these power laws are often taken as an unambiguous means to differentiate between diffusive, viscous, and ballistic transport. Our finding highlights that Fermi surface geometry and orientation can act as confounding factors when differentiating between transport regimes. Here we observed that predominantly ballistic electron dynamics lead to behaviour close to the expected $\omega^{2/3}$ dependence in one orientation, but in another orientation lead to behaviour much closer to the $\omega^{1/2}$ dependence typically associated with diffusive dynamics. This indicates that in DC experiments, orientation-dependent differences from the canonical quadratic relationship between conductance and width in the ballistic regime are likely to be seen in width-restricted channel experiments performed in carefully oriented channels.

The success of our AC Boltzmann transport theory in turn enables extension of this kind of study to other ultra-high-conductivity materials with known Fermi surfaces, and prediction of the non-local AC transport effects likely to be found in them. Experimentally, we have demonstrated the utility of broadband microwave spectroscopy in the investigation of non-local electrodynamics. While the foundational measurements of the ASE were performed at fixed frequencies [16–18, 34], in the present work, continuous-frequency measurements were critical to the interpretation of our results: in particular, in identifying a ballistic- rather than viscous-dominated regime, and in revealing the predicted breakdown of Pippard theory as a result of a strongly-faceted Fermi surface. These effects are also technologically relevant, as future applications of ultra-high-conductivity materials are likely to operate at GHz frequencies. The ASE is known to limit the conductance of interconnects in integrated circuits when operated at these high frequencies [46]. The present results demonstrate that conductance can be improved by aligning interconnects along a direction for which the ASE is suppressed. Finally, to our knowledge, our findings represent the first experimental observation of the ASE outside of elemental metals, suggesting experimental opportunities among new-generation ultra-high-conductivity materials. The interplay of frequency, scattering rates, carrier density, and Fermi surface geometry gives rise to a rich phenomenological landscape for non-local electrodynamics, particularly in the microwave and terahertz range—which, to date, remains largely unexplored [47–52].

ACKNOWLEDGMENTS

We are grateful to Alex Levchenko for helpful discussions. G.B., T.W.B., J.D., M.H., and D.A.B. acknowledge support from the Max Planck-UBC-UTokyo Center for Quantum Materials and the Canada First Research Excellence Fund, Quantum Materials and Future Technologies Program, as well as the Natural Sciences

and Engineering Research Council of Canada (RGPIN-2018-04280). D. V. acknowledges partial support by the Swiss National Science Foundation (SNSF) through the SNSF Early Postdoc. Mobility Grant P2GEP2_18145. D.V. and J.S. acknowledge support by the European Commission’s Horizon 2020 RISE program Hydrotronics (Grant No. 873028). P.S. acknowledges the support of the Narodowe Centrum Nauki (NCN) Sonata Bis grant 2019/34/E/ST3/00405 and the Nederlandse Organisatie voor Wetenschappelijk Onderzoek (NWO) Klein grant via NWA route 2. Y.M. acknowledges the support by JSPS KAKENHI JP22H01168. The work in Dresden was in part supported by the Deutsche Forschungsgemeinschaft (DFG) through the Würzburg-Dresden Cluster of Excellence on Complexity and Topology in Quantum Matter – ct.qmat (EXC 2147, project ID 39085490) and the Leibniz Prize programme.

-
- [1] K. G. Nazaryan and L. Levitov, Robustness of vorticity in electron fluids, [arXiv:2111.09878](#) (2021).
- [2] L. W. Molenkamp and M. J. M. de Jong, Electron-electron-scattering-induced size effects in a two-dimensional wire, [Physical Review B](#) **49**, 5038 (1994).
- [3] M. J. M. De Jong and L. W. Molenkamp, Hydrodynamic electron flow in high-mobility wires, [Physical Review B](#) **51**, 13389 (1995).
- [4] C. Q. Cook and A. Lucas, Electron hydrodynamics with a polygonal Fermi surface, [Physical Review B](#) **99**, 235148 (2019).
- [5] G. Varnavides, A. S. Jermyn, P. Anikeeva, C. Felser, and P. Narang, Electron hydrodynamics in anisotropic materials, [Nature Communications](#) **11**, 4710 (2020).
- [6] C. Q. Cook and A. Lucas, Viscometry of Electron Fluids from Symmetry, [Physical Review Letters](#) **127**, 176603 (2021).
- [7] M. Qi and A. Lucas, Distinguishing viscous, ballistic, and diffusive current flows in anisotropic metals, [Physical Review B](#) **104**, 195106 (2021).
- [8] P. J. Turner, D. M. Broun, S. Kamal, M. E. Hayden, J. S. Bobowski, R. Harris, D. C. Morgan, J. S. Preston, D. A. Bonn, and W. N. Hardy, Bolometric technique for high-resolution broadband microwave spectroscopy of ultra-low-loss samples, [Review of Scientific Instruments](#) **75**, 124 (2004).
- [9] W. A. Huttema, B. Morgan, P. J. Turner, W. N. Hardy, X. Zhou, D. A. Bonn, R. Liang, and D. M. Broun, Apparatus for high-resolution microwave spectroscopy in strong magnetic fields, [Review of Scientific Instruments](#) **77**, 023901 (2006).
- [10] D. Bonn and W. Hardy, Microwave Electrodynamics of High Temperature Superconductors, in [Handbook of High-Temperature Superconductivity: Theory and Experiment](#) (2007) pp. 145–214.
- [11] Y. Matsuda, N. P. Ong, Y. F. Yan, J. M. Harris, and J. B. Peterson, Vortex viscosity in $\text{YBa}_2\text{Cu}_3\text{O}_{7-\delta}$ at low temperatures, [Physical Review B](#) **49**, 4380 (1994).
- [12] J. C. Booth, D. H. Wu, and S. M. Anlage, A broadband method for the measurement of the surface impedance of thin films at microwave frequencies, [Review of Scientific Instruments](#) **65**, 2082 (1994).
- [13] G. E. H. Reuter and E. H. Sondheimer, The theory of the anomalous skin effect in metals, [Proceedings of the Royal Society A](#) **195**, 336 (1948).
- [14] E. H. Sondheimer, The Theory of the Anomalous Skin Effect in Anisotropic Metals, [Proceedings of the Royal Society A](#) **224**, 260 (1954).
- [15] A. Pippard, The anomalous skin effect in anisotropic metals, [Proceedings of the Royal Society A](#) **224**, 273 (1954).
- [16] A. Pippard, The surface impedance of superconductors and normal metals at high frequencies II. The anomalous skin effect in normal metals, [Proceedings of the Royal Society A](#) **191**, 385 (1947).
- [17] R. G. Chambers, Anomalous Skin Effect in Metals, [Nature](#) **165**, 289 (1950).
- [18] R. G. Chambers, The anomalous skin effect, [Proceedings of the Royal Society A](#) **215**, 481 (1952).
- [19] G. Smith, Anomalous Skin Effect in Bismuth, [Physical Review](#) **115**, 1561 (1959).
- [20] R. N. Gurzhi, Hydrodynamic effects in solids at low temperature, [Soviet Physics Uspekhi](#) **11**, 255 (1968).
- [21] A. P. Mackenzie, R. K. Haselwimmer, A. W. Tyler, G. G. Lonzarich, Y. Mori, S. Nishizaki, and Y. Maeno, Extremely Strong Dependence of Superconductivity on Disorder in Sr_2RuO_4 , [Physical Review Letters](#) **80**, 161 (1998).
- [22] M. E. Barber, A. S. Gibbs, Y. Maeno, A. P. Mackenzie, and C. W. Hicks, Resistivity in the Vicinity of a van Hove Singularity: Sr_2RuO_4 under Uniaxial Pressure, [Physical Review Letters](#) **120**, 76602 (2018).
- [23] See Supplemental Material at [URL will be inserted by publisher].
- [24] N. Ashcroft and N. Mermin, *Solid State Physics* (Holt-Saunders, 1976).
- [25] C. W. Hicks, A. S. Gibbs, A. P. Mackenzie, H. Takatsu, Y. Maeno, and E. A. Yelland, Quantum Oscillations and High Carrier Mobility in the Delafossite PdCoO_2 , [Physical Review Letters](#) **109**, 116401 (2012).
- [26] V. Sunko, P. H. McGuinness, C. S. Chang, E. Zhakina, S. Khim, C. E. Dreyer, M. Konczykowski, H. Bormann, P. J. W. Moll, M. König, D. A. Müller, and A. P. Mackenzie, Controlled Introduction of Defects to Delafossite Metals by Electron Irradiation, [Physical Review X](#) **10**, 021018 (2020).
- [27] P. J. W. Moll, P. Kushwaha, N. Nandi, B. Schmidt, and A. P. Mackenzie, Evidence for hydrodynamic electron flow in PdCoO_2 , [Science](#) **351**, 1061 (2016).
- [28] H.-J. Noh, J. Jeong, J. Jeong, E.-J. Cho, S. B. Kim, K. Kim, B. I. Min, and H.-D. Kim, Anisotropic Electric Conductivity of Delafossite PdCoO_2 Studied by Angle-Resolved Photoemission Spectroscopy, [Physical Review Letters](#) **102**, 256404 (2009).
- [29] V. Sunko, H. Rosner, P. Kushwaha, S. Khim, F. Mazzola, L. Bawden, O. J. Clark, J. M. Riley, D. Kasinathan, M. W. Haverkort, T. K. Kim, M. Hoesch, J. Fujii, I. Vobornik, A. P. Mackenzie, and P. D. King, Maximal Rashba-like spin splitting via kinetic-energy-coupled inversion-symmetry breaking, [Nature](#) **549**, 492 (2017).
- [30] M. D. Bachmann, A. L. Sharpe, A. W. Barnard, C. Putzke, M. König, S. Khim, D. Goldhaber-Gordon, A. P. Mackenzie, and P. J. W. Moll, Super-geometric electron focusing on the hexagonal Fermi surface of PdCoO_2 , [Nature Communications](#) **10**, 5081 (2019).
- [31] P. H. McGuinness, E. Zhakina, M. König, M. D. Bachmann, C. Putzke, P. J. W. Moll, S. Khim, and A. P. Mackenzie, Low-symmetry nonlocal transport in microstructured squares of delafossite metals, [Proceedings of the National Academy of Sciences](#) **118**, 2113185118 (2021).
- [32] M. D. Bachmann, A. L. Sharpe, G. Baker, A. W. Barnard, C. Putzke, T. Scaffidi, N. Nandi, P. H. McGuinness, E. Zhakina, M. Moravec, S. Khim, M. König, D. Goldhaber-Gordon, A. P. Mackenzie, and P. J. W. Moll, Directional ballistic transport in the two-dimensional metal PdCoO_2 , [Nature Physics](#) **10.1038/s41567-022-01570-7** (2022).
- [33] U. Frisch, B. Hasslacher, and Y. Pomeau, Lattice-gas Automata for the Navier-Stokes Equation, [Physical Review Letters](#) **56**, 1505 (1986).
- [34] A. Pippard, An Experimental Determination of the Fermi

- Surface in Copper, [Philosophical Transactions of the Royal Society A](#) **250**, 325 (1957).
- [35] M. L. Glasser, Influence of Band Structure on the Non-local Conductivity of Metals and the Anomalous Skin Effect, [Physical Review](#) **176**, 1110 (1968).
- [36] M. I. Kaganov and P. Contreras, Theory of the anomalous skin effect in metals with complicated Fermi surfaces, [Journal of Experimental and Theoretical Physics](#) **79**, 985 (1994).
- [37] N. A. Zimbovskaya, Local features of the Fermi surface curvature and the anomalous skin effect in metals, [Journal of Physics: Condensed Matter](#) **18**, 8149 (2006).
- [38] T. Harada, K. Fujiwara, and A. Tsukazaki, Highly conductive PdCoO₂ ultrathin films for transparent electrodes, [APL Materials](#) **6**, 046107 (2018).
- [39] M. Brahlek, G. Rimal, J. M. Ok, D. Mukherjee, A. R. Mazza, Q. Lu, H. N. Lee, T. Zac Ward, R. R. Unocic, G. Eres, and S. Oh, Growth of metallic delafossite PdCoO₂ by molecular beam epitaxy, [Physical Review Materials](#) **3**, 093401 (2019).
- [40] J. Sun, M. R. Barone, C. S. Chang, M. E. Holtz, H. Paik, J. Schubert, D. A. Muller, and D. G. Schlom, Growth of PdCoO₂ by ozone-assisted molecular-beam epitaxy, [APL Materials](#) **7**, 121112 (2019).
- [41] A. P. Mackenzie, The properties of ultrapure delafossite metals, [Reports on Progress in Physics](#) **80**, 32501 (2017).
- [42] Y. Wang, G. Varnavides, P. Anikeeva, J. Gooth, C. Felser, and P. Narang, Generalized Design Principles for Hydrodynamic Electron Transport in Anisotropic Metals, [arXiv:2109.00550](#) (2021).
- [43] A. Levchenko and J. Schmalian, Transport properties of strongly coupled electron-phonon liquids, [Annals of Physics](#) **419**, 168218 (2020).
- [44] X. Huang and A. Lucas, Electron-phonon hydrodynamics, [Physical Review B](#) **103**, 155128 (2021).
- [45] A. Hui, S. Lederer, V. Oganessian, and E.-A. Kim, Quantum aspects of hydrodynamic transport from weak electron-impurity scattering, [Physical Review B](#) **101**, 121107 (2020).
- [46] R. Sarvari, *Impact of Size Effects and Anomalous Skin Effect on Metallic Wires as GSI Interconnects*, Ph.D. thesis, Georgia Institute of Technology (2008).
- [47] H. B. G. Casimir and J. Ubbink, The skin effect II. The skin effect at high frequencies, [Philips Technical Review](#) **28**, 300 (1967).
- [48] D. Forcella, J. Zaanen, D. Valentinis, and D. van der Marel, Electromagnetic properties of viscous charged fluids, [Physical Review B](#) **90**, 035143 (2014).
- [49] D. Valentinis, J. Zaanen, and D. Van Der Marel, Propagation of shear stress in strongly interacting metallic Fermi liquids enhances transmission of terahertz radiation, [Scientific Reports](#) **11**, 7105 (2021).
- [50] D. Valentinis, Optical signatures of shear collective modes in strongly interacting Fermi liquids, [Physical Review Research](#) **3**, 023076 (2021).
- [51] P. Matus, R. M. A. Dantas, R. Moessner, and P. Surówka, Skin effect as a probe of transport regimes in Weyl semimetals, [Proceedings of the National Academy of Sciences](#) **119**, e2200367119 (2022).
- [52] D. Valentinis, G. Baker, D. A. Bonn, and J. Schmalian, Kinetic theory of the non-local electrodynamic response in anisotropic metals: skin effect in 2D systems, [arXiv:2204.13344](#) (2022).

Supplemental material:
Non-local electrodynamics in ultra-pure PdCoO₂
(Dated: March 2, 2023)

CONTENTS

S1. Sr ₂ RuO ₄ preparation & analysis	1
S2. Sn preparation & analysis	6
S3. PdCoO ₂ preparation & analysis	6
S4. PdCoO ₂ surface resistance calculations	10
S5. Estimate of momentum-conserving electron-phonon scattering in PdCoO ₂	13
References	15

S1. Sr₂RuO₄ PREPARATION & ANALYSIS

A. Preparation

The Sr₂RuO₄ sample was grown in an image furnace by the floating-zone method [1, 2]. The as-grown crystals are typically 5 to 8 cm long rods and $2 \times 3 \text{ mm}^2$ in cross-section with the crystallographic c axis oriented perpendicular to the long axis of the rod. Samples were prepared by first cutting a 1 to 2 mm section from the as-grown rod using a diamond saw. Platelet samples, approximately 50 μm thick, were then cleaved from the cut section such that the broad faces were aligned with the ab planes.

The highest-quality Sr₂RuO₄ single crystals have a sharp superconducting transition with a maximum transition temperature of $T_c = 1.50 \text{ K}$. AC susceptibility measurements are used to characterize the superconducting transitions of Sr₂RuO₄ crystals and gauge the sample quality [3, 4]. The sample used in this study had a 25 mK wide superconducting transition with $T_c = 1.41 \text{ K}$. The sharpness of the transition is a clear indication of the high-purity of the sample. The suboptimal T_c is likely due to a nonstoichiometric Ru content in the platelet sample.

During the floating-zone growth, some RuO₂ is lost to evaporation such that excess RuO₂ is required when preparing the the initial feed rod. On the other hand, during the crystal growth, excessive RuO₂ leads to Ru segregation and the formation of a eutectic phase that causes internal strain and an enhanced T_c (the so-called 3-K phase) [5, 6]. It is, therefore, necessary to balance these two effects when preparing the initial feed rod. For the floating-zone growth conditions used at Kyoto University, 15% excess RuO₂ in the feed rod has been found to be near optimal [1, 2]. The sample used in this study did not show any signs of the 3-K phase.

B. Classical Skin Effect fit

The measured data were fit to

$$R = A\omega^{1/2} \quad (1)$$

yielding a value of $A = 7.5 \times 10^{-8} \Omega \text{ Hz}^{-1/2}$. In our measurement, the microwave-frequency magnetic field was applied parallel to the ab plane of a platelet sample, inducing current both in the ab plane and along the c axis of Sr₂RuO₄'s tetragonal crystal structure. When the skin depth is small compared to sample dimensions, the measured surface resistance can be expressed as

$$R = f_{ab}R_{ab} + f_cR_c \quad (2)$$

where $f_i = A_i / \sum_j A_j$ and A_i is the area of faces in which currents run in the i direction. Our sample dimensions, given in Fig. S1 and Table S1, were such that current ran predominantly in the ab plane, with $f_{ab} = 0.94$ and $f_c = 0.06$

[7]. In the Classical Skin Effect (CSE), surface resistance for current in the i direction is given by

$$R_i = \sqrt{\frac{\mu_0 \omega \rho_i}{2}} \quad (3)$$

where ρ_i is the corresponding DC resistivity. Defining the resistivity anisotropy as $\alpha \equiv \rho_c / \rho_{ab}$ gives

$$R = (f_{ab} + \sqrt{\alpha} f_c) R_{ab} \quad (4)$$

such that

$$\rho_{ab} = \frac{2}{\mu_0} \left(\frac{A}{f_{ab} + \sqrt{\alpha} f_c} \right)^2. \quad (5)$$

To determine ρ_{ab} from our fit, we must assume a value for α . Reported values of α in the literature range from 400 to 4000 [8], yielding a range from 38 to 185 nΩ cm for the ρ_{ab} value of our sample. Recently reported residual resistivity values are 100 nΩ cm for ρ_{ab} [9] and 0.228 and 0.278 mΩ cm for ρ_c [10], giving $\alpha = 2280$ and 2780. Using these values of α in Eq. (5) gives $\rho_{ab} = 59$ and 50 nΩ cm, leading to our reported value of approximately 50 nΩ cm in the main text.

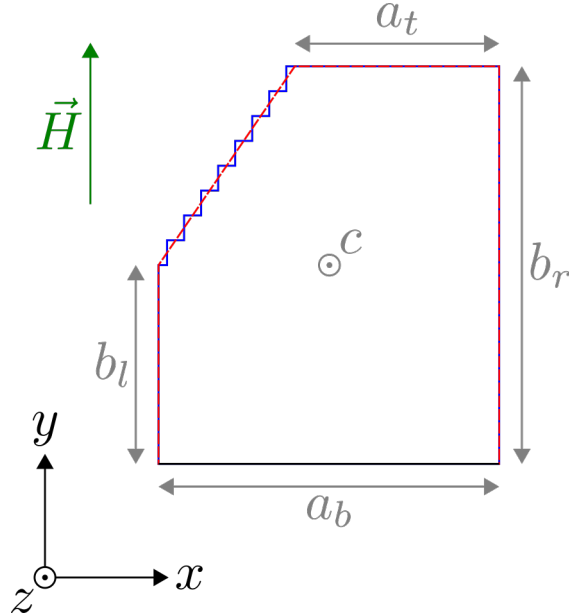


FIG. S1. Geometry of Sr_2RuO_4 sample and alignment of microwave-frequency magnetic field. The idealized sample geometry is shown in red. The discretized sample geometry, as used in the extended fit of Section S1 C, is shown in blue. The sample dimensions are given in Table S1.

Dimension	Value [μm]
a_b	900
a_t	540
b_l	525
b_r	1050
c	46

TABLE S1. Dimensions of Sr_2RuO_4 sample. Labels refer to Fig. S1.

C. Corrections to $\sqrt{\omega}$ behavior

The Sr_2RuO_4 data exhibit small yet systematic deviations from $\sqrt{\omega}$ power-law behavior. Here, we show that these deviations are well-described by corrections coming from two effects: (1) the electromagnetic finite size effect—an

extrinsic effect due to sample geometry—and (2) proximity to the relaxation regime. Both of these corrections fall within the scope of conventional, local electrodynamics, and do not change our interpretation of the data as arising from diffusive electron dynamics within the skin layer.

Here, we develop a model to account for these corrections in our Sr_2RuO_4 sample. To lay the groundwork for describing the full model, we start by reviewing the known solution for a simpler geometry. We consider an infinitely-long anisotropic metal with rectangular cross-section with dimensions a and c . We consider a spatially-uniform, AC magnetic field with magnitude H_0 which is applied along the infinite dimension of the sample. We consider an effective surface impedance, defined so that the average power absorbed per unit area is $Z_{\text{eff}} H_0^2 / 2$. Assuming local electrodynamics, the effective surface impedance is given by [11][12]

$$Z_{\text{eff}}^{\text{rect}}(a, c) = i\mu_0\omega\tilde{\delta}_{\text{eff}} \quad (6)$$

with

$$\tilde{\delta}_{\text{eff}} = \frac{ac}{a+c} \frac{4}{\pi^2} \sum_{\text{odd } n > 0} \frac{1}{n^2} \left(\frac{\tanh \alpha_n}{\alpha_n} + \frac{\tanh \beta_n}{\beta_n} \right) \quad (7)$$

where

$$\alpha_n = \frac{c}{2\tilde{\delta}_a} \left[1 + \left(\frac{n\pi\tilde{\delta}_c}{a} \right)^2 \right]^{1/2} \quad (8)$$

and

$$\beta_n = \frac{a}{2\tilde{\delta}_c} \left[1 + \left(\frac{n\pi\tilde{\delta}_a}{c} \right)^2 \right]^{1/2}. \quad (9)$$

The complex skin depth for current flowing along direction i is given by

$$\tilde{\delta}_i = \sqrt{\frac{1}{i\mu_0\omega\sigma_i(\omega)}} \quad (10)$$

where $\sigma_i(\omega)$ is the frequency-dependent conductivity in that direction.

For our Sr_2RuO_4 sample, the dimension along the x axis is a function of the z coordinate (see Fig. S1). We may approximate the effective surface impedance of our sample by discretizing its geometry in terms of slices of rectangular cross-section [13]. Assuming that the tangential magnetic field has a magnitude of H_0 at each slice, the effective surface impedance is then given by

$$Z_{\text{eff}} = \sum_i Z_{\text{eff}}^{\text{rect}}(a_i, c) \cdot \frac{b_i}{\sum_i b_i} \quad (11)$$

where the factor $b_i / \sum_i b_i$ weights the contribution of each slice by its length along the y axis. To capture relaxation effects, we assume a Drude conductivity

$$\sigma_i^{\text{Drude}} = \frac{1/\rho_i}{1 + i\omega/\gamma_{\text{mr},i}} \quad (12)$$

and, for simplicity, take $\gamma_{\text{mr},ab} = \gamma_{\text{mr},c} \equiv \gamma_{\text{mr}}$.

Using the above model, we performed a fit to the Sr_2RuO_4 surface resistance data with three free parameters: ρ_{ab} , ρ_c , and γ_{mr} . The number of slices was increased until the fit parameters converged; this was achieved by nine slices, as shown in Fig. S1. The fit is shown in Fig. S2 and fit parameters are given in Table S2. Both the $\sqrt{\omega}$ and extended fit yield similar values of ρ_{ab} . While the difference between the two fits is difficult to distinguish on a log-log plot (Fig. S2(a)), the superiority of the extended fit becomes visible upon dividing the data by $\sqrt{\omega}$ (Fig. S2(b)). Even so, the data deviate from the $\sqrt{\omega}$ fit by less than $\pm 5\%$. Figure S2(c) & (d) illustrate that, while there is a correction to $\sqrt{\omega}$ behavior owing to proximity to a crossover to the relaxation regime, the data are nonetheless below the frequency at which the relaxation regime is entered.

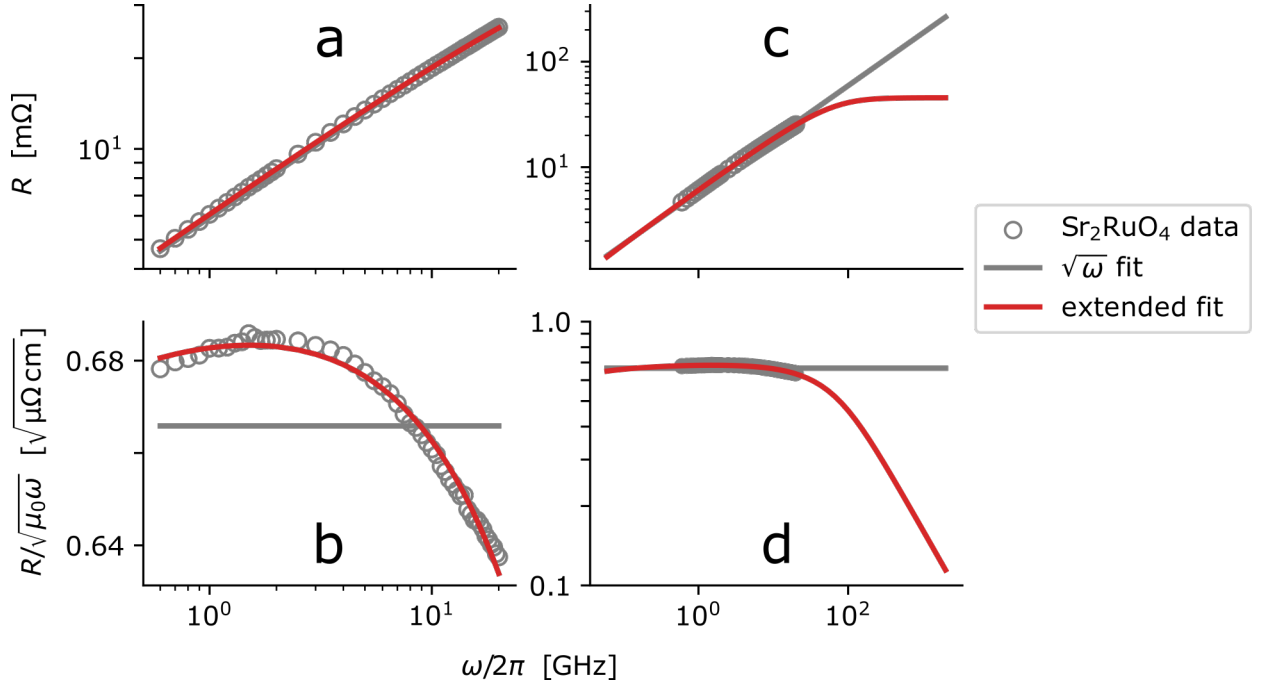


FIG. S2. Fit of Sr_2RuO_4 to the extended surface resistance model, including corrections to $\sqrt{\omega}$ behavior. (a) The $\sqrt{\omega}$ and extended-model fits are difficult to distinguish on a log-log plot of surface resistance R versus frequency ω . (b) Upon dividing R by $\sqrt{\omega}$, it can be seen that the extended fit is superior. (c), (d) Examining the extended fit over a wider frequency range shows that, despite the correction to $\sqrt{\omega}$ behavior stemming from relaxation effects, the data are below the frequency regime where these effects dominate the behavior of the surface resistance.

Parameter	Value
ρ_{ab}	64.2 nΩ cm
ρ_c	99.8 μΩ cm
γ_{mr}	680 GHz

TABLE S2. Best-fit parameters for the fit of the Sr_2RuO_4 data to the extended model.

D. Verification of expectation of Classical Skin Effect

We wish to confirm that, according to conventional theory of the CSE and Anomalous Skin Effect (ASE) [14, 15], we should expect to observe the CSE. We will do so by determining the expected location of the crossover to the ASE. We note that we have already empirically determined the location of the expected crossover to the relaxation regime in Section S1C; from our fit we have that $\omega_{c \leftrightarrow r}/2\pi = \gamma_{\text{mr}}/2\pi = 108$ GHz, which is indeed outside of our measurement range.

Because Sr_2RuO_4 is tetragonal, the appropriate pre-existing model of the ASE is that for spheroidal Fermi surfaces within the relaxation time approximation, as considered by Sondheimer [15] in a follow-up to the original work on spherical Fermi surfaces by Reuter and Sondheimer [14]. For an electronic dispersion given by

$$\mathcal{E}_{\mathbf{k}} = \frac{\hbar^2}{2m_a}(k_x^2 + k_y^2) + \frac{\hbar^2}{2m_c}k_z^2, \quad (13)$$

the classical surface impedance is

$$Z_i^c = \left[\frac{1}{\sigma_{0,ii}} \mu_0 \omega \right]^{1/2} e^{-i\pi/4} = \left[\frac{1}{\epsilon_0 \omega_{p,ii}^2 \tau} \mu_0 \omega \right]^{1/2} e^{-i\pi/4} \quad (14)$$

and the anomalous surface impedance is

$$Z_{i,j}^a = \beta \left[\frac{\sqrt{3}}{2\pi} \frac{l_j}{\sigma_{0,ii}} (\mu_0 \omega^2) \right]^{1/3} e^{-i\pi/3} = \beta \left[\frac{\sqrt{3}}{2\pi} \frac{v_j}{\epsilon_0 \omega_{p,ii}^2} (\mu_0 \omega^2) \right]^{1/3} e^{-i\pi/3} \quad (15)$$

where the following definitions have been used:

$$\sigma_{0,ii} = \epsilon_0 \omega_{p,ii}^2 \tau \quad (16)$$

$$\epsilon_0 \omega_{p,ii}^2 = \frac{ne^2}{m_i} = \frac{k_a^2 k_c}{3\pi^2} \frac{e^2}{m_i} \quad (17)$$

$$k_i^2 = \frac{2m_i \mathcal{E}_F}{\hbar^2} \quad (18)$$

$$v_i = \frac{\hbar k_i}{m_i} = \sqrt{\frac{2\mathcal{E}_F}{m_i}} \quad (19)$$

$$l_i = v_i \tau. \quad (20)$$

We see that the resistivity anisotropy is related to the various quantities of interest via

$$\alpha \equiv \frac{\rho_c}{\rho_a} = \frac{\sigma_{0,aa}}{\sigma_{0,cc}} = \frac{m_c}{m_a} = \frac{\omega_{p,aa}^2}{\omega_{p,cc}^2} = \frac{v_a^2}{v_c^2} = \frac{l_a^2}{l_c^2}. \quad (21)$$

While the location of the crossover from CSE to ASE can be estimated by the condition $\delta = l$, a more precise determination of the crossover frequency comes from equating the surface resistances in the two regimes. This leads to a crossover frequency given by

$$\omega_{c \leftrightarrow a} = \frac{32\pi^2}{3\mu_0 \sigma_{0,ii} l_j^2} \quad (22)$$

where i indicates the current direction and j indicates the wavevector direction. Along the large faces of our platelet sample, current is in the a direction and wavevector is along the c direction; on the smaller side faces, current is along the c direction and wavevector is along the a direction. Because in the spheroidal model $\sigma_{0,aa} l_c^2 = \sigma_{0,cc} l_a^2$, the same crossover frequency applies for all faces in our measurement.

In reality, Sr_2RuO_4 is known to have three Fermi surface sheets. In order to apply the spheroidal model to calculate $\omega_{c \leftrightarrow a}$, we must determine the quantity $\sigma_{0,cc} l_a^2$ (or $\sigma_{0,aa} l_c^2$) for an equivalent spheroidal Fermi surface. We use the material parameters from Ref. [16], as listed in Table S3. Following Ref. [16], the in-plane mean free path and conductivity in Sr_2RuO_4 can be related via

$$l_a = C_1 \sigma_{0,aa} \quad (23)$$

with

$$C_1 \equiv \frac{\hbar d}{e^2 \sum_n k_F^{(n)}} \quad (24)$$

where $d = 6.4 \text{ \AA}$ is the inter-layer spacing. Using Eqs. (21) and (23) we can write

$$\sigma_{0,cc} l_a^2 = \frac{C_1^2}{\alpha} \sigma_{0,aa}^3. \quad (25)$$

We can then obtain the crossover frequency using our experimentally-determined value of $\sigma_{0,aa} = 1/\rho_{ab} = 1/50 \text{ n}\Omega \text{ cm}$ and the corresponding value of $\alpha = 2780$:

$$\frac{\omega_{c \leftrightarrow a}}{2\pi} = \frac{1}{2\pi} \frac{32\pi^2}{3\mu_0} \left(\frac{C_1^2}{\alpha} \sigma_{0,aa}^3 \right)^{-1} \approx 5 \text{ THz}. \quad (26)$$

We see that we should not expect to observe the crossover from CSE to ASE according to conventional theory.

Sheet	k_F (\AA^{-1})	m^* (m_e)	v_F (10^6 m/s)
α	0.30	3.2	0.11
β	0.62	6.6	0.11
γ	0.75	12	0.072

TABLE S3. Fermi surface parameters for Sr_2RuO_4 . The parameters k_F and m^* come from Ref. [16], while v_F was calculated using $v_F = \hbar k_F / m^*$.

S2. Sn PREPARATION & ANALYSIS

A. Preparation

The polycrystalline, platelet sample of Sn was prepared by cold-rolling 99.99% pure Sn to the desired thickness and then cutting the lateral dimensions with a razor blade.

B. Anomalous Skin Effect fit

To fit the Sn data, we used the original theory of the ASE developed by Reuter and Sondheimer [14]. It is based on the assumption of an isotropic, three-dimensional, free-electron dispersion. The asymptotic expression for the surface resistance in the ASE regime can be expressed as

$$R = \left(\frac{3\sqrt{3}\pi\hbar^3\mu_0^2\omega^2}{16e^2m_e^2v_F^2} \right)^{1/3} \quad (27)$$

where we have assumed that electrons scatter diffusely from the sample's surface and have a band mass equal to the free electron mass m_e . We fit the Sn data to Eq. (27) with the Fermi velocity v_F as the only free parameter.

C. Verification of expectation of Anomalous Skin Effect

Here, we wish to verify that we would expect to observe the ASE in Sn according to standard theory. As discussed in the main text, in order to observe the ASE over our entire frequency range, the classical skin depth must be less than the momentum-relaxing (MR) mean free path over the entire frequency range of the experimental measurements: $\delta_{\text{cl}} < \lambda_{\text{mr}}$. A more precise but less physically insightful condition is that the asymptotic CSE surface resistance R_{cse} should be greater than the asymptotic ASE surface resistance over the entire experimental frequency range: $R_{\text{cse}} > R_{\text{ase}}$. An upper bound on the DC resistivity comes from meeting this criterion at our lowest measured frequency. Using Eqs. (14) and (27) to rewrite the inequality in terms of resistivity, we find

$$\rho < \frac{2A^2\omega_{\text{min}}^{1/3}}{\mu_0} \approx 20 \text{ n}\Omega \text{ cm} \quad (28)$$

where we have used the experimentally-determined value of A to evaluate the expression. We cannot deduce the DC resistivity of our sample directly from our measurement—a remarkable property of the ASE is that the asymptotic value of the surface resistance becomes independent of the DC resistivity [17]. Therefore, we turn to reported resistivity values for Sn to assess whether the inequality expressed in Eq. (28) can reasonably be met. In Ref. [17], the resistivities of two Sn samples from different commercial sources were reported to be 2 and 7 n Ω cm at 4.2 K. This suggests that it is indeed reasonable for the inequality expressed in Eq. (28) to be achieved at our measurement temperature of 5.0 K.

S3. PdCoO₂ PREPARATION & ANALYSIS

A. Preparation

Single crystals of PdCoO₂ were grown using a mixture of PdCl₂ and CoO using the following methathetical reaction in an evacuated quartz ampule: $\text{PdCl}_2 + 2\text{CoO} \rightarrow 2\text{PdCoO}_2 + \text{CoCl}_2$. The ampule was heated to 1000 °C for 12 h

and then to between 700 and 750 °C for 5 d. The product was washed and distilled with water and ethanol to remove CoCl_2 .

Platelet samples were cut into hexagons using a high-precision wire saw with a 50 μm tungsten wire and 50 nm Al_2O_3 abrasive suspended in glycerin. The orientation of the crystals was determined via their growth edges, which are oriented perpendicular to the crystallographic axes. A goniometer mounted to the wire saw was used to rotate the samples in between cuts. Samples 1 and 2 were cut from the same original crystal. For Sample 3, a smaller thickness was desired, so it was cut from a separate crystal from the same batch. The sample dimensions listed in Table S4 were determined via optical microscopy and were used for the data analysis in Section S3.

Sample	Hexagonal face area [mm^2]	Hexagonal face perimeter [mm]	Thickness [μm]	Cut orientation
1	0.187	1.72	88	$a \parallel y$
2	0.169	1.62	79	$a \parallel x$
3	0.191	1.76	49	$a \parallel x$

TABLE S4. Geometry of PdCoO_2 samples. The cut orientations refer to the directions defined in Figure 2 of the main text.

B. Raw surface resistance

To quantitatively interpret the measurements, it is necessary to account for the extrinsic geometric effects which lead to a difference between the externally applied, spatially-uniform magnetic field \mathbf{H}_0 and the magnetic field $\mathbf{H}(\mathbf{r})$ at the sample's surface. Consider a sample characterized by two dimensions: c , parallel to \mathbf{H}_0 , and a , perpendicular to \mathbf{H}_0 . In a conductor for which the skin depth $\delta \ll \{c, a\}$, eddy currents will act such that at the sample's surface, $\mathbf{H}(\mathbf{r})$ is nearly parallel to the surface. For a sample with $c \gg a$, $H(\mathbf{r}) \approx H_0$ at the sample's surface. However, for $c < a$, as in the present work, $H(\mathbf{r})$ will have a non-trivial variation over the sample's surface. This effect is well-known in the context of magnetization measurements, where it is common practice to account for extrinsic geometric effects using demagnetization factors [18]. In this work, we measured the power dissipated by the sample. In analogy with demagnetization factors, here we examine “power factors” to account for extrinsic geometric effects in our measurements of power absorption. A similar concept has been invoked previously in Refs. [19, 20].

The time-averaged power dissipated in a sample is equal to the mean electromagnetic energy entering the sample per unit time:

$$P = \int \bar{\mathbf{S}} \cdot d\mathbf{A} = \frac{1}{2} \text{Re} \left[\int dA E_t \times H_t^* \right] = \frac{1}{2} R_{\text{raw}} \int dA H_t^2 \quad (29)$$

where $\bar{\mathbf{S}}$ is the time-averaged Poynting vector, E_t and H_t are the magnitudes of the tangential fields at the sample's surface, and R_{raw} is the sample's effective surface resistance. When $\delta \ll \{c, a\}$, the variation of H_t^2 over the sample's surface is that of a perfect conductor of the same shape and is independent of absolute sample size [20]. Therefore, we define the power factor for a given sample shape as

$$\alpha \equiv \frac{1}{AH_0^2} \int H_t^2 dA \quad (30)$$

where H_t is the tangential magnetic field strength experienced by a perfect conductor of the same shape. The surface resistances reported in Fig. 2(d) of the main text were found from measurements of power dissipation via

$$R_{\text{raw}} = \frac{2P}{\alpha AH_0^2}. \quad (31)$$

H_0 is the magnitude of the applied magnetic field, as determined via an in-situ reference sample, and A is the sample's surface area.

To confirm the validity of taking $\delta \ll \{c, a\}$, we have estimated the skin depth across the range of measured frequencies using the classical expression and the published ab -plane residual resistivity of 7.5 n Ω cm [21]. We find that the classical skin depth is always $< 0.1 \mu\text{m}$, and thus always more than two orders of magnitude less than the smallest sample dimension.

We studied the power factor α as a function of sample aspect ratio c/a for several different shapes, as shown in Fig. S3. For spheroids, it was possible to treat the problem analytically [22]. For cylinders and hexagonal prisms,

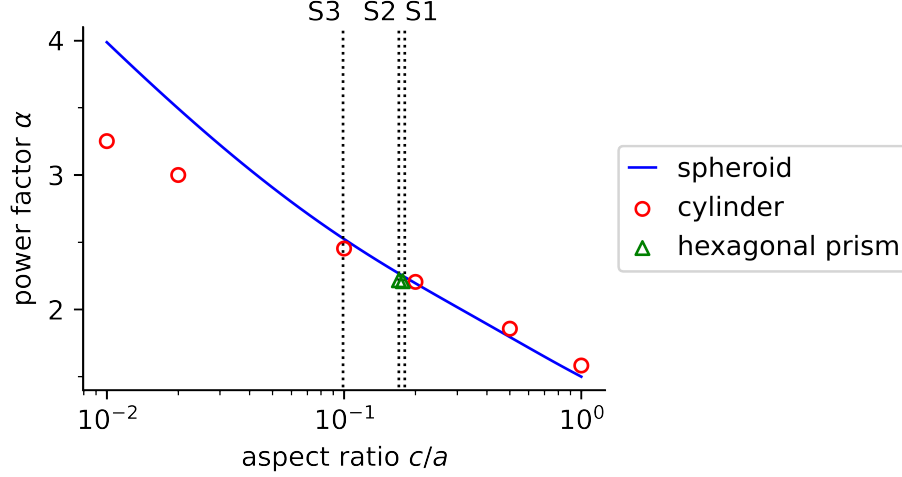


FIG. S3. Effect of sample geometry on overall power absorption.

finite-element simulations were performed [23]. Because the axial symmetry of cylinders allows for faster convergence of simulation results, this shape was studied over a wide range of aspect ratios. Since the simulation of hexagonal prisms was more resource-intensive, we only focused on directly relevant aspect ratios. Within the range of aspect ratios relevant to the samples studied here, all three shapes yielded similar results.

C. Surface resistance components

Because $\delta \ll \{c, a\}$, R_{raw} can be viewed as a sum of two independent components: R_{\perp} comes from the faces perpendicular to \mathbf{H}_0 (the two large hexagonal faces) and R_{\parallel} comes from the faces parallel to \mathbf{H}_0 (the six small rectangular faces). The relative contribution of the two components is set by a weight w_{\perp} :

$$R_{\text{raw}} = w_{\perp} R_{\perp} + (1 - w_{\perp}) R_{\parallel} \quad (32)$$

The weight w_{\perp} can be found via the variation of the tangential magnetic field strength over the surface of a perfect conductor of the same shape:

$$w_{\perp} = \frac{\int_{A_{\perp}} H_t^2 dA}{\int_{A_{\perp} + A_{\parallel}} H_t^2 dA} \quad (33)$$

where A_{\perp} (A_{\parallel}) is the area of the perpendicular (parallel) faces. The weights determined by our finite-element simulations are shown in Fig. S4.

Applying Eq. (32) to the three samples that we measured, we get

$$R_1 = w_1 R_{a,c} + (1 - w_1) R_{30,0} \quad (34)$$

$$R_2 = w_2 R_{a,c} + (1 - w_2) R_{0,30} \quad (35)$$

$$R_3 = w_3 R_{a,c} + (1 - w_3) R_{0,30} \quad (36)$$

where on the left side of the equations, R_i refers to R^{eff} for Sample i , and on the right side of the equations, the two subscripts refer to the directions $\hat{\mathbf{J}}, \hat{\mathbf{q}}$. Using Eqs. (35) and (36), $R_{a,c}$ was found from the measurements of Samples 2 and 3:

$$R_{a,c} = \frac{w_2 R_3 - w_3 R_2}{w_2(1 - w_3) - (1 - w_2)w_3}. \quad (37)$$

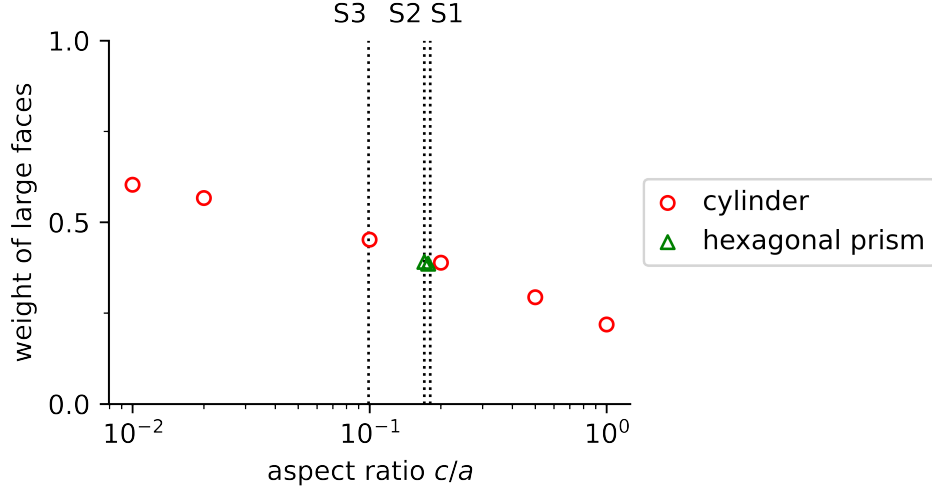


FIG. S4. Effect of sample geometry on relative contribution of faces.

$R_{a,c}$ was then used to determine $R_{30,0}$ and $R_{0,30}$ from Eqs. (34) and (35):

$$R_{30,0} = \frac{R_1 - w_1}{1 - w_1} \quad (38)$$

$$R_{0,30} = \frac{R_2 - w_2 R_{a,c}}{1 - w_2}. \quad (39)$$

The values of α and w_\perp that were used in Eqs. (31) and (37) to (39) to arrive at the data presented in the main text are summarized in Table S5. For Samples 1 and 2, we used the values of α and w_\perp from our simulations. For Sample 3, some adjustment relative to the simulation values was necessary in order to obtain physically plausible results for the components $R_{a,c}$, $R_{30,0}$, and $R_{0,30}$. We found that the magnitude of R_3 determined using the simulation value α_3^{sim} was larger than expected. Specifically, unless R_3 is of a comparable magnitude to R_2 , then the decomposition into components via Eqs. (37) to (39) yields negative values, which is unphysical. A comparable magnitude of R_3 to R_2 can be accomplished by using $\alpha_3 \approx 4$, whereas the simulation value is $\alpha_3^{\text{sim}} \approx 2.5$. There are a couple potential explanations for this discrepancy. The first is that Sample 3, being cut from a different original sample, has a higher residual MR scattering rate than Sample 2. In the CSE, $R \propto \sqrt{\gamma_{\text{mr}}}$, so a factor of $4/2.5 \approx 1.6$ difference in magnitude corresponds to a factor of $1.6^2 \approx 2.6$ difference in residual scattering rates. This is consistent with the variation in residual resistivity reported by Nandi *et al.* [24]. The second potential explanation is that we failed to accurately account for geometric effects in our simulations, with α_3^{sim} being smaller than the true value of α_3 . This difference in magnitude would result if the power factor α increases more rapidly with decreasing aspect ratio c/a than captured by our simulations. With α_3 set to 4, next we turned to w_3 . The simulation value of ≈ 0.45 also leads to negative decomposed values, whereas there is a wide range of w_3 values near ≈ 0.6 for which the decomposed values are positive and only weakly dependent on the specific choice of w_3 . As with α , the difference between empirical and simulated results may indicate that simulations are underestimating the magnitude of extrinsic geometric effects for small aspect ratios. Despite the necessity to adjust α_3 and w_3 relative to simulation values to get physically reasonable results, the resulting values of $R_{a,c}$, $R_{30,0}$, and $R_{0,30}$ vary little over the range of (α_3, w_3) pairs leading to physically plausible results.

Sample	α	w_\perp
1	2	0.4
2	2	0.4
3	4	0.6

TABLE S5. Data calibration parameters.

S4. PdCoO₂ SURFACE RESISTANCE CALCULATIONS

Here we describe the details of the PdCoO₂ surface resistance calculations shown in the main text. First, we describe a generalized treatment of non-local electrodynamics that allows for arbitrary Fermi surface geometry and separate MR and momentum-conserving (MC) scattering rates. Then, we describe the application of this treatment to PdCoO₂.

A. Distribution function

We start with the Boltzmann equation for the evolution of the electronic distribution function $f_{\mathbf{k}}(\mathbf{r}, t)$ in the presence of a spatially- and time-varying electric field $\mathbf{E}(\mathbf{r}, t)$:

$$\left[\frac{\partial}{\partial t} + \dot{\mathbf{r}} \cdot \nabla_{\mathbf{r}} + \dot{\mathbf{k}} \cdot \nabla_{\mathbf{k}} \right] f_{\mathbf{k}}(\mathbf{r}, t) = -\mathcal{C}_{\mathbf{k}}[f_{\mathbf{k}}(\mathbf{r}, t)] \quad (40)$$

with semi-classical equations of motion

$$\dot{\mathbf{r}} = \mathbf{v}_{\mathbf{k}} = \frac{1}{\hbar} \nabla_{\mathbf{k}} \mathcal{E}_{\mathbf{k}} \quad (41)$$

and

$$\dot{\mathbf{k}} = -\frac{e}{\hbar} \mathbf{E}(\mathbf{r}, t) \quad (42)$$

and where $\mathcal{C}_{\mathbf{k}}[f_{\mathbf{k}}]$ is the collision integral. We expand the distribution function around its equilibrium value f_0 :

$$f_{\mathbf{k}} = f_0 + w_{\mathbf{k}} \psi_{\mathbf{k}} \quad (43)$$

with

$$w_{\mathbf{k}} = k_B T \left(-\frac{\partial f_0}{\partial \mathcal{E}_{\mathbf{k}}} \right) = f_0(1 - f_0). \quad (44)$$

We take the Fourier transform of Eq. (40) and keep terms to linear order in $\psi_{\mathbf{k}}$ to obtain

$$[-i\omega + i\mathbf{v}_{\mathbf{k}} \cdot \mathbf{q}] \psi_{\mathbf{k}}(\mathbf{q}, \omega) + \frac{e}{k_B T} \mathbf{E}(\mathbf{q}, \omega) \cdot \mathbf{v}_{\mathbf{k}} = -\hat{\mathcal{C}}_{\mathbf{k}} \psi_{\mathbf{k}}(\mathbf{q}, \omega) \quad (45)$$

where $\hat{\mathcal{C}}$ is the linearized collision operator

$$\hat{\mathcal{C}} \psi_{\mathbf{k}} = \frac{1}{w_{\mathbf{k}}} \int_{\mathbf{k}'} \frac{\delta \mathcal{C}_{\mathbf{k}}}{\delta \psi_{\mathbf{k}'}} \psi_{\mathbf{k}'}. \quad (46)$$

Let $\psi_{\mathbf{k}}$ be an element of a function space with inner product

$$\langle \phi | \psi \rangle = \int_{\mathbf{k}} w_{\mathbf{k}} \phi_{\mathbf{k}}^* \psi_{\mathbf{k}}. \quad (47)$$

We use as a basis the complete and orthonormal set of eigenfunctions $\chi_{\mathbf{k}, m}$ of the collision operator:

$$\hat{\mathcal{C}} \chi_{\mathbf{k}, m} = \gamma_{\mathbf{k}, m} \chi_{\mathbf{k}, m} \quad (48)$$

with

$$\sum_m |\chi_{\mathbf{k}, m}\rangle \langle \chi_{\mathbf{k}, m}| = 1 \quad (49)$$

and

$$\langle \chi_{\mathbf{k}, m} | \chi_{\mathbf{k}, m'} \rangle = \delta_{m, m'}. \quad (50)$$

We assume that the eigenfunctions $\chi_{\mathbf{k},m}$ include

$$\chi_{\mathbf{k},0} = c_0 \quad (51)$$

and

$$\chi_{\mathbf{k},i} = c_i c_0 \hat{v}_{\mathbf{k},i} \quad (52)$$

where $i \in \{x, y, z\}$ and that the eigenvalue spectrum is given by

$$\gamma_{\mathbf{k},m} = \begin{cases} 0 & m = 0 \\ \gamma_{\mathbf{k},i}^{\text{mr}} & m = i \\ \gamma_{\mathbf{k}}^{\text{mc}} & \text{otherwise.} \end{cases} \quad (53)$$

This describes a scenario in which collisions conserve charge, relax momentum in the i direction at a rate $\gamma_{\mathbf{k},i}^{\text{mr}}$, and relax all other modes at a rate $\gamma_{\mathbf{k}}^{\text{mc}}$. Using Eq. (49), we may write the collision operator as

$$\hat{C} = \gamma_{\mathbf{k}}^{\text{mc}}(1 - |\chi_{\mathbf{k},0}\rangle \langle \chi_{\mathbf{k},0}|) - \sum_i \delta\gamma_{\mathbf{k},i} |\chi_{\mathbf{k},i}\rangle \langle \chi_{\mathbf{k},i}| \quad (54)$$

where $\delta\gamma_{\mathbf{k},i} \equiv \gamma_{\mathbf{k}}^{\text{mc}} - \gamma_{\mathbf{k},i}^{\text{mr}}$.

Throughout, we will use

$$\int_{\mathbf{k}} \dots \equiv \frac{2}{(2\pi)^d} \int d\mathbf{k} \dots = \frac{2}{(2\pi)^d \hbar} \int_0^\infty d\mathcal{E} \int_{\mathcal{S}(\mathcal{E})} \frac{dS}{v_{\mathbf{k}}} \dots \quad (55)$$

Furthermore, we will assume that $T \ll T_F$ such that

$$\int_{\mathbf{k}} -\frac{\partial f_0}{\partial \mathcal{E}_{\mathbf{k}}} \dots = \frac{2}{(2\pi)^d \hbar} \int_{S_F} \frac{dS}{v_{\mathbf{k}}} \dots \quad (56)$$

where S_F is the Fermi surface $\mathcal{S}(\mathcal{E}_{\mathbf{k}} = \mathcal{E}_F)$. Finally, for simplicity, we will assume that on the Fermi surface the magnitude of the velocity is isotropic: $v_{\mathbf{k}} = v_F \hat{v}_{\mathbf{k}}$ for \mathbf{k} on S_F .

The constants c_0 and c_i are determined by Eq. (50). We find

$$\frac{1}{c_0^2} = \frac{2k_B T}{(2\pi)^d \hbar v_F} S_F \quad (57)$$

and

$$\frac{1}{c_i^2} = \int_{S_F} \frac{dS}{S_F} \hat{v}_{\mathbf{k},i}^2 \quad (58)$$

where

$$S_F \equiv \int_{S_F} dS. \quad (59)$$

We can now rewrite the collision integral as

$$\hat{C}\psi_{\mathbf{k}} = \gamma_{\mathbf{k}}^{\text{mc}}\psi_{\mathbf{k}} - \gamma_{\mathbf{k}}^{\text{mc}}n_0 - \sum_i c_i^2 \delta\gamma_{\mathbf{k},i} \hat{v}_{\mathbf{k},i} p_i \quad (60)$$

where

$$n_0 \equiv \int_{S_F} \frac{dS}{S_F} \psi_{\mathbf{k}} \quad (61)$$

and

$$p_i \equiv \int_{S_F} \frac{dS}{S_F} \hat{v}_{\mathbf{k},i} \psi_{\mathbf{k}} \quad (62)$$

The solution to the Boltzmann equation is then

$$\psi_{\mathbf{k}}(\mathbf{q}, \omega) = \frac{-\frac{e}{k_B T} \mathbf{E}(\mathbf{q}, \omega) \cdot \mathbf{v}_{\mathbf{k}} + \gamma_{\mathbf{k}}^{\text{mc}} n_0(\mathbf{q}, \omega) + \sum_i c_i^2 \delta\gamma_{\mathbf{k},i} \hat{v}_{\mathbf{k}i} p_i(\mathbf{q}, \omega)}{\gamma_{\mathbf{k}}^{\text{mc}} - i\omega + i\mathbf{v}_{\mathbf{k}} \cdot \mathbf{q}}. \quad (63)$$

Because we are ultimately interested in finding the transverse conductivity, we take $\mathbf{E} \perp \mathbf{q}$ with $\mathbf{E} \parallel \hat{\boldsymbol{\alpha}}$ and $\mathbf{q} \parallel \hat{\boldsymbol{\beta}}$. We define

$$\langle \mathcal{A} \rangle \equiv \int_{S_F} \frac{dS}{S_F} \frac{\mathcal{A}}{\gamma_{\mathbf{k}}^{\text{mc}} - i\omega + i\mathbf{v}_F \hat{\mathbf{v}}_{\mathbf{k}\beta} q}. \quad (64)$$

We find that

$$\begin{pmatrix} \gamma_{\mathbf{k}}^{\text{mc}} \langle 1 \rangle - 1 & c_{\beta}^2 \delta\gamma_{\mathbf{k},\beta} \langle \hat{v}_{\mathbf{k}\beta} \rangle & c_{\alpha}^2 \delta\gamma_{\mathbf{k},\alpha} \langle \hat{v}_{\mathbf{k}\alpha} \rangle & c_{\gamma}^2 \delta\gamma_{\mathbf{k},\gamma} \langle \hat{v}_{\mathbf{k}\gamma} \rangle \\ \gamma_{\mathbf{k}}^{\text{mc}} \langle \hat{v}_{\mathbf{k}\beta} \rangle & c_{\beta}^2 \delta\gamma_{\mathbf{k},\beta} \langle \hat{v}_{\mathbf{k}\beta}^2 \rangle - 1 & c_{\alpha}^2 \delta\gamma_{\mathbf{k},\alpha} \langle \hat{v}_{\mathbf{k}\beta} \hat{v}_{\mathbf{k}\alpha} \rangle & c_{\gamma}^2 \delta\gamma_{\mathbf{k},\gamma} \langle \hat{v}_{\mathbf{k}\beta} \hat{v}_{\mathbf{k}\gamma} \rangle \\ \gamma_{\mathbf{k}}^{\text{mc}} \langle \hat{v}_{\mathbf{k}\alpha} \rangle & c_{\beta}^2 \delta\gamma_{\mathbf{k},\beta} \langle \hat{v}_{\mathbf{k}\alpha} \hat{v}_{\mathbf{k}\beta} \rangle & c_{\alpha}^2 \delta\gamma_{\mathbf{k},\alpha} \langle \hat{v}_{\mathbf{v}\alpha}^2 \rangle - 1 & c_{\gamma}^2 \delta\gamma_{\mathbf{k},\gamma} \langle \hat{v}_{\mathbf{k}\alpha} \hat{v}_{\mathbf{k}\gamma} \rangle \\ \gamma_{\mathbf{k}}^{\text{mc}} \langle \hat{v}_{\mathbf{k}\gamma} \rangle & c_{\beta}^2 \delta\gamma_{\mathbf{k},\beta} \langle \hat{v}_{\mathbf{k}\gamma} \hat{v}_{\mathbf{k}\beta} \rangle & c_{\alpha}^2 \delta\gamma_{\mathbf{k},\alpha} \langle \hat{v}_{\mathbf{k}\gamma} \hat{v}_{\mathbf{k}\alpha} \rangle & c_{\gamma}^2 \delta\gamma_{\mathbf{k},\gamma} \langle \hat{v}_{\mathbf{k}\gamma}^2 \rangle - 1 \end{pmatrix} \begin{pmatrix} n_0 \\ p_{\beta} \\ p_{\alpha} \\ p_{\gamma} \end{pmatrix} = \frac{e}{k_B T} E_y v_F \begin{pmatrix} \langle \hat{v}_{\mathbf{k}\alpha} \rangle \\ \langle \hat{v}_{\mathbf{k}\beta} \hat{v}_{\mathbf{k}\alpha} \rangle \\ \langle \hat{v}_{\mathbf{k}\alpha}^2 \rangle \\ \langle \hat{v}_{\mathbf{k}\gamma} \hat{v}_{\mathbf{k}\alpha} \rangle \end{pmatrix} \quad (65)$$

and assuming three mirror planes, we get

$$\begin{pmatrix} \gamma_{\mathbf{k}}^{\text{mc}} \langle 1 \rangle - 1 & c_{\beta}^2 \delta\gamma_{\mathbf{k},\beta} \langle \hat{v}_{\mathbf{k}\beta} \rangle & 0 & 0 \\ \gamma_{\mathbf{k}}^{\text{mc}} \langle \hat{v}_{\mathbf{k}\beta} \rangle & c_{\beta}^2 \delta\gamma_{\mathbf{k},\beta} \langle \hat{v}_{\mathbf{k}\beta}^2 \rangle - 1 & 0 & 0 \\ 0 & 0 & c_{\alpha}^2 \delta\gamma_{\mathbf{k},\alpha} \langle \hat{v}_{\mathbf{v}\alpha}^2 \rangle - 1 & 0 \\ 0 & 0 & 0 & c_{\gamma}^2 \delta\gamma_{\mathbf{k},\gamma} \langle \hat{v}_{\mathbf{k}\gamma}^2 \rangle - 1 \end{pmatrix} \begin{pmatrix} n_0 \\ p_{\beta} \\ p_{\alpha} \\ p_{\gamma} \end{pmatrix} = \frac{e}{k_B T} E_y v_F \begin{pmatrix} 0 \\ 0 \\ \langle \hat{v}_{\mathbf{k}\alpha}^2 \rangle \\ 0 \end{pmatrix} \quad (66)$$

To ensure that $\psi_{\mathbf{k}} = 0$ when $\mathbf{E} = 0$, we must also have $n_0 = p_{\beta} = 0$. For p_{α} we have

$$p_{\alpha} = -\frac{eE v_F}{k_B T} \frac{\langle \hat{v}_{\mathbf{k}\alpha}^2 \rangle}{1 - c_{\alpha}^2 \delta\gamma_{\mathbf{k},\alpha} \langle \hat{v}_{\mathbf{k}\alpha}^2 \rangle} \quad (67)$$

so that

$$\psi_{\mathbf{k}} = -\frac{eE v_F}{k_B T} \frac{1}{\gamma_{\mathbf{k}}^{\text{mc}} - i\omega + i\mathbf{q} v_F \hat{\mathbf{v}}_{\mathbf{k}\beta}} \frac{\hat{v}_{\mathbf{k}\alpha}}{1 - c_{\gamma}^2 \delta\gamma_{\mathbf{k},\alpha} \langle \hat{v}_{\mathbf{k}\alpha}^2 \rangle}. \quad (68)$$

B. Non-local transverse conductivity

Electrical current is given by

$$\mathbf{J} = -e \int_{\mathbf{k}} \mathbf{v}_{\mathbf{k}} f_{\mathbf{k}}. \quad (69)$$

Using

$$J_i(\mathbf{q}, \omega) = \sigma_{ij}(\mathbf{q}, \omega) E_j(\mathbf{q}, \omega) \quad (70)$$

and assuming $\delta\gamma_{\mathbf{k},\alpha}$ to be \mathbf{k} -independent, we find the non-local transverse conductivity for $\mathbf{E} \parallel \hat{\boldsymbol{\alpha}}$ and $\mathbf{q} \parallel \hat{\boldsymbol{\beta}}$ as

$$\sigma(q, \omega) = \epsilon_0 \Omega_p^2 \frac{G_0(q, \omega)}{1 - c_{\alpha}^2 \delta\gamma_{\alpha} G_0(q, \omega)} \quad (71)$$

where

$$G_0(q, \omega) \equiv \langle \hat{v}_{\mathbf{k}\alpha}^2 \rangle = \int_{S_F} \frac{dS}{S_F} \frac{\hat{v}_{\mathbf{k}\alpha}^2}{\gamma_{\mathbf{k}}^{\text{mc}} - i\omega + i\mathbf{q} v_F \hat{\mathbf{v}}_{\mathbf{k}\beta}}. \quad (72)$$

and

$$\Omega_p^2 \equiv \sum_i \omega_{p,i}^2 \quad (73)$$

where plasma frequency is given by

$$\epsilon_0 \omega_{p,i}^2 = \frac{e^2 v_F^2}{c_0^2 k_B T} \int_{S_F} \frac{dS}{S_F} \hat{v}_{\mathbf{k}i}^2. \quad (74)$$

C. Parameterization of Fermi surface

For a Fermi surface \mathcal{S}_F parametrized by the Fermi vector $\mathbf{k}_F(g, h)$ with $g \in \{g_1, g_2\}$ and $h \in \{h_1, h_2\}$, we define the vector \mathbf{n} as

$$\mathbf{n}(g, h) = \frac{\partial \mathbf{k}_F(g, h)}{\partial g} \times \frac{\partial \mathbf{k}_F(g, h)}{\partial h}. \quad (75)$$

Then the Fermi surface integral is given by

$$\int_{\mathcal{S}_F} dS \dots = \int_{g_1}^{g_2} dg \int_{h_1}^{h_2} dh n(g, h) \dots \quad (76)$$

with $n \equiv |\mathbf{n}|$. The unit vector normal to the Fermi surface (parallel to the Fermi velocity) is given by

$$\hat{\mathbf{n}}(g, h) = \frac{\mathbf{n}(g, h)}{n(g, h)}. \quad (77)$$

D. Surface resistance

For specular scattering of electrons at the sample's surface, surface impedance is given by [14]

$$Z = i\mu_0\omega \frac{2}{\pi} \int_0^\infty dq \left[i\mu_0\omega\sigma(q, \omega) + \frac{\omega^2}{c^2} - q^2 \right]^{-1} \quad (78)$$

while for diffuse scattering, it is given by [25]

$$Z = i\mu_0\omega\pi \left(\int_0^\infty dq \ln \left[\frac{i\mu_0\omega\sigma(q, \omega)}{q^2} + \frac{\omega^2}{c^2q^2} - 1 \right] \right)^{-1}. \quad (79)$$

Finally, surface resistance is given by

$$R = \text{Re}(Z). \quad (80)$$

E. Calculations for PdCoO₂

We used the Fermi surface parameterization from Hicks *et al.* [21]:

$$\mathbf{k}_F(\phi, \phi_0, k_z) = \rho(\phi - \phi_0, k_z) [\cos \phi \hat{\mathbf{i}} + \sin \phi \hat{\mathbf{j}}] + k_z \hat{\mathbf{k}} \quad (81)$$

where

$$\rho(\phi - \phi_0, k_z) = \sum_{\mu, \nu} k_{\mu\nu} \cos[\mu(\phi - \phi_0)] \begin{cases} \sin[\nu dk_z] & k_{31} \\ \cos[\nu dk_z] & \text{otherwise} \end{cases} \quad (82)$$

with $d = c/3$ where $c = 17.743 \text{ \AA}$ and with the Fermi surface harmonics listed in Table S6. The angle ϕ_0 sets the in-plane rotation of the Fermi surface relative to the coordinate system. To take advantage of the simplifications arising from three mirror planes, we set $k_{31} = 0$. We assumed diffuse surface scattering when calculating the surface resistance. We used the reported experimental parameters as given in Table S7. We took $\gamma_{\mathbf{k}x}^{\text{mr}} = \gamma_{\mathbf{k}x}^{\text{mr}} = \gamma^{\text{mr}}$ using the value from Table S7, and took $\gamma_{\mathbf{k}}^{\text{mc}} = \gamma^{\text{mc}}$ with γ^{mc} as a free parameter.

S5. ESTIMATE OF MOMENTUM-CONSERVING ELECTRON-PHONON SCATTERING IN PdCoO₂

Here we estimate the rate of MC electron-phonon scattering in PdCoO₂. First, we obtained an experimental MR scattering rate as $\gamma_1^{\text{exp}} = \rho_{xx}/\epsilon_0\omega_{p,xx}^2$ using ρ_{xx} for a 155 μm channel from Nandi *et al.* [24] and using $\omega_{p,xx} = 7.2 \times 10^{15} \text{ Hz}$ from Hicks *et al.* [21]. Next, we performed fits to γ_1^{exp} . The results are shown in Fig. S5 and the fit

μ	ν	$k_{\mu,\nu}$
0	0	0.9538
6	0	0.040
12	0	0.007
0	1	0.0107
0	2	-0.009
3	1	0.0010

TABLE S6. Harmonics for parameterization of Fermi surface of PdCoO₂ from Hicks *et al.* [21].

Parameter	Value
v_F	7.5×10^5 m/s
$\omega_{p,ab}$	7.2×10^{15} Hz
$\rho_{ab}(T = 2 \text{ K})$	7.5 nΩ cm
$\gamma^{\text{mr}}(T = 2 \text{ K})$	34 GHz

TABLE S7. Parameters for PdCoO₂. All parameters are directly from Hicks *et al.* [21], except for γ^{mr} which was found as $\gamma^{\text{mr}} = \epsilon_0 \omega_{p,ab}^2 \rho_{ab}$.

parameters given in Table S8. To find the MR electron-impurity scattering rate γ_1^{imp} , we fit γ_1^{exp} to a constant over the range $2 \text{ K} < T < 10 \text{ K}$. Next we considered electron-phonon scattering. It has previously been noted that at high temperature $\gamma_1^{\text{exp}} \propto T^\alpha$ with $\alpha > 1$, in contrast with expectation that $\alpha = 1$ within the Bloch-Grüneisen treatment of electron-acoustic phonon scattering. This discrepancy has been attributed to electron-optical phonon scattering [21, 26]. Therefore, we fit $\gamma_1^{\text{exp}} - \gamma_1^{\text{imp}}$ to a sum of Einstein and Debye contributions using

$$\hbar\gamma_1^{\text{Ein}} = \frac{\pi}{2} \lambda_E k_B T_E \frac{T_E/T}{\sinh^2(T_E/2T)} \quad (83)$$

and

$$\hbar\gamma_l^{\text{Deb}} = 4\pi\lambda_D k_B T \left(\frac{T}{T_D}\right)^2 \int_0^{T_D/T} dx \frac{x^3}{\cosh(x) - 1} [1 - P_l(1 - (T/T_D)^2 x^2)] \quad (84)$$

with $l = 1$ (cf. eq. A.45 from Levchenko and Schmalian [27]). The fit returned Debye and Einstein temperatures T_D and T_E and transport electron-phonon couplings λ_D and λ_E . Following Hicks *et al.* [21], the fit was performed over the range $60 \text{ K} < T < 300 \text{ K}$. Having determined T_D and λ_D , we then used Eq. (84) to determine γ_l^{Debye} for all l , as shown in Fig. S6. We see that at 2 K, all γ_l for electron-Debye phonon scattering are less than the experimentally determined MR scattering rate. Therefore, electron-phonon scattering is unlikely to be responsible for the MC scattering inferred from our measurements.

γ_1^{imp}	39 GHz
λ_D	0.049
T_D	331 K
λ_E	0.030
T_E	1120 K

TABLE S8. Parameters for fit of momentum-relaxing scattering rate in PdCoO₂.

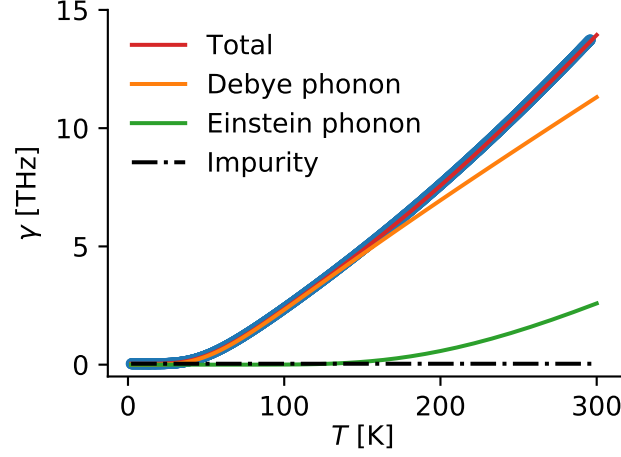


FIG. S5. Fit of momentum-relaxing scattering rate in PdCoO₂ showing the contribution of each scattering mechanism. The data (in blue) were obtained from bulk resistivity measurements.

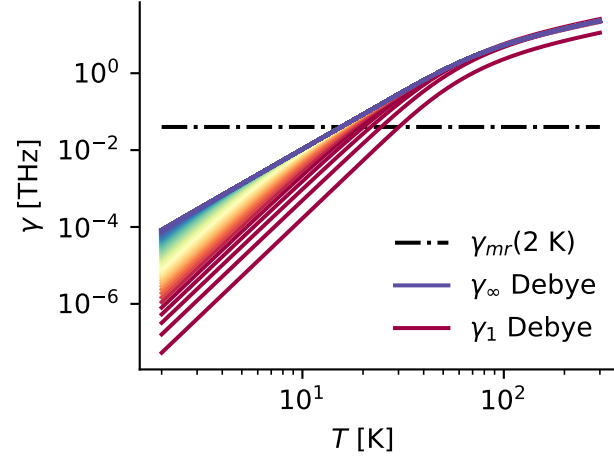


FIG. S6. Spectrum of scattering rates for electron-Debye phonon scattering compared with the 2 K momentum-relaxing scattering rate.

-
- [1] Z. Q. Mao, Y. Maenoab, and H. Fukazawa, Crystal growth of Sr₂RuO₄, [Materials Research Bulletin](#) **35**, 1813 (2000).
 - [2] J. S. Bobowski, N. Kikugawa, T. Miyoshi, H. Suwa, H. S. Xu, S. Yonezawa, D. A. Sokolov, A. P. Mackenzie, and Y. Maeno, Improved single-crystal growth of Sr₂RuO₄, [Condensed Matter](#) **4**, 6 (2019).
 - [3] S. Yonezawa, T. Higuchi, Y. Sugimoto, C. Sow, and Y. Maeno, Compact AC susceptometer for fast sample characterization down to 0.1 K, [Review of Scientific Instruments](#) **86**, 093903 (2015).
 - [4] C. P. Bidinosti and W. N. Hardy, High precision ac susceptometer for measuring the temperature and magnetic field dependence of the penetration depth in superconductor single crystals, [Review of Scientific Instruments](#) **71**, 3816 (2000).
 - [5] Y. Maeno, T. Ando, Y. Mori, E. Ohmichi, S. Ikeda, S. Nishizaki, and S. Nakatsuji, Enhancement of superconductivity of Sr₂RuO₄ to 3 K by embedded metallic microdomains, [Physical Review Letters](#) **81**, 3765 (1998).
 - [6] C. W. Hicks, D. O. Brodsky, E. a. Yelland, A. S. Gibbs, J. a. N. Bruin, M. E. Barber, S. D. Eddins, K. Nishimura, S. Yonezawa, Y. Maeno, and A. P. Mackenzie, Strong Increase of T_c of Sr₂RuO₄ Under Both Tensile and Compressive Strain, [Science](#) **344**, 283 (2014).
 - [7] We took $A_{ab} = 2(a_b b_r - (b_r - b_l)(a_b - a_t)/2)$ and $A_c = (b_l + \sqrt{(b_r - b_l)^2 + (a_b - a_t)^2} + b_r)c$.
 - [8] C. Bergemann, A. P. Mackenzie, S. R. Julian, D. Forsythe, and E. Ohmichi, Quasi-two-dimensional Fermi liquid properties of the unconventional superconductor Sr₂RuO₄, [Advances in Physics](#) **52**, 639 (2003).

- [9] M. E. Barber, A. S. Gibbs, Y. Maeno, A. P. Mackenzie, and C. W. Hicks, Resistivity in the Vicinity of a van Hove Singularity: Sr_2RuO_4 under Uniaxial Pressure, [Physical Review Letters](#) **120**, 76602 (2018).
- [10] F. Jerzembeck, H. S. Røising, A. Steppke, H. Rosner, D. A. Sokolov, N. Kikugawa, T. Scaffidi, S. H. Simon, A. P. Mackenzie, and C. W. Hicks, The superconductivity of Sr_2RuO_4 under c -axis uniaxial stress, [Nature Communications](#) **13**, 4596 (2022).
- [11] D. M. Broun, *The Microwave Electrodynamics of Unconventional Superconductors*, Ph.D. thesis (2000).
- [12] In Section [S1 C](#) only, the formulae implicitly reflect a sign choice of $\exp(+i\omega t)$ time dependence so as to match Ref. [11]. Everywhere else, the formulae implicitly reflect a sign choice of $\exp(-i\omega t)$ time dependence.
- [13] A. Haug, *Microwave response of the heavy-fermion superconductor CeCu_2Si_2* , Ph.D. thesis (2019).
- [14] G. E. H. Reuter and E. H. Sondheimer, The theory of the anomalous skin effect in metals, [Proceedings of the Royal Society A](#) **195**, 336 (1948).
- [15] E. H. Sondheimer, The Theory of the Anomalous Skin Effect in Anisotropic Metals, [Proceedings of the Royal Society A](#) **224**, 260 (1954).
- [16] A. P. Mackenzie, S. R. Julian, A. J. Diver, G. G. Lonzarich, N. E. Hussey, Y. Maeno, S. Nishizaki, and T. Fujita, Calculation of thermodynamic and transport properties of Sr_2RuO_4 at low temperatures using known Fermi surface parameters, [Physica C: Superconductivity and its Applications](#) **263**, 510 (1996).
- [17] A. Pippard, The surface impedance of superconductors and normal metals at high frequencies II. The anomalous skin effect in normal metals, [Proceedings of the Royal Society A](#) **191**, 385 (1947).
- [18] R. Prozorov and V. G. Kogan, Effective Demagnetizing Factors of Diamagnetic Samples of Various Shapes, [Physical Review Applied](#) **10**, 14030 (2018).
- [19] T. H. Fawzi, K. F. Ali, and P. E. Burke, Eddy current losses in finite length conducting cylinders, [IEEE Transactions on Magnetics](#) **19**, 2216 (1983).
- [20] L. D. Landau and E. M. Lifshitz, Chapter VII, in *Electrodynamics of Continuous Media* (Pergamon, 1984) 2nd ed., Chap. VII, pp. 199–224.
- [21] C. W. Hicks, A. S. Gibbs, A. P. Mackenzie, H. Takatsu, Y. Maeno, and E. A. Yelland, Quantum Oscillations and High Carrier Mobility in the Delafossite PdCoO_2 , [Physical Review Letters](#) **109**, 116401 (2012).
- [22] G. Baker, *Non-local electrical conductivity in PdCoO_2* , Ph.D. thesis, University of British Columbia (2022).
- [23] T. W. Branch, *Microwave Responses of Strongly Demagnetized Metallic Samples*, Master’s thesis, University of British Columbia (2021).
- [24] N. Nandi, T. Scaffidi, P. Kushwaha, S. Khim, M. E. Barber, V. Sunko, F. Mazzola, P. D. C. King, H. Rosner, P. J. W. Moll, M. König, J. E. Moore, S. Hartnoll, and A. P. Mackenzie, Unconventional magneto-transport in ultrapure PdCoO_2 and PtCoO_2 , [npj Quantum Materials](#) **3**, 66 (2018).
- [25] R. Dingle, The anomalous skin effect and the reflectivity of metals I., [Physica](#) **19**, 311 (1953).
- [26] H. Takatsu, S. Yonezawa, S. Mouri, S. Nakatsuji, K. Tanaka, and Y. Maeno, Roles of high-frequency optical phonons in the physical properties of the conductive delafossite PdCoO_2 , [Journal of the Physical Society of Japan](#) **76**, 104701 (2007).
- [27] A. Levchenko and J. Schmalian, Transport properties of strongly coupled electron–phonon liquids, [Annals of Physics](#) **419**, 168218 (2020).